

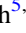





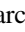
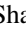
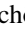
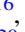


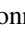



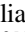

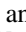




The K2 Galactic Archaeology Program Data Release 2: Asteroseismic Results from Campaigns 4, 6, and 7

Joel C. Zinn^{1,2,3} , Dennis Stello^{1,4,5,6} , Yvonne Elsworth^{5,7} , Rafael A. García⁸ , Thomas Kallinger⁹ , Savita Mathur^{10,11,12} ,
Benôit Mosser¹³ , Lisa Bugnet^{8,14} , Caitlin Jones⁷ , Marc Hon¹⁵ , Sanjib Sharma^{4,6} , Ralph Schönrich¹⁶ ,
Jack T. Warfield^{2,17} , Rodrigo Luger^{18,19} , Marc H. Pinsonneault² , Jennifer A. Johnson² , Daniel Huber²⁰ ,
Victor Silva Aguirre⁵ , William J. Chaplin^{5,7} , Guy R. Davies^{5,7} , and Andrea Miglio^{5,7} 

¹ Department of Astrophysics, American Museum of Natural History, Central Park West at 79th Street, New York, NY 10024, USA; jzinn@amnh.org

² School of Physics, University of New South Wales, Barker Street, Sydney, NSW 2052, Australia

³ Department of Astronomy, The Ohio State University, 140 West 18th Avenue, Columbus OH 43210, USA

⁴ Sydney Institute for Astronomy (SIfA), School of Physics, University of Sydney, NSW 2006, Australia

⁵ Stellar Astrophysics Centre, Department of Physics and Astronomy, Aarhus University, Ny Munkegade 120, DK-8000 Aarhus C, Denmark

⁶ Center of Excellence for Astrophysics in Three Dimensions (ASTRO-3D), Australia

⁷ School of Physics and Astronomy, University of Birmingham, Edgbaston, Birmingham, B15 2TT, UK

⁸ AIM, CEA, CNRS, Université Paris-Saclay, Université Paris Diderot, Sorbonne Paris Cité, F-91191 Gif-sur-Yvette, France

⁹ Institute of Astrophysics, University of Vienna, Türkenschanzstrasse 17, Vienna A-1180, Austria

¹⁰ Space Science Institute, 4750 Walnut Street Suite #205, Boulder, CO 80301, USA

¹¹ Instituto de Astrofísica de Canarias, La Laguna, Tenerife, Spain

¹² Dpto. de Astrofísica, Universidad de La Laguna, La Laguna, Tenerife, Spain

¹³ LESIA, Observatoire de Paris, PSL Research University, CNRS, Sorbonne Université, Université de Paris Diderot, F-92195 Meudon, France

¹⁴ IRFU, CEA, Université Paris-Saclay, F-91191 Gif-sur-Yvette, France

¹⁵ School of Physics, University of New South Wales, Barker Street, Sydney, NSW 2052, Australia

¹⁶ Mullard Space Science Laboratory, University College London, Holmbury St Mary, Dorking RH5 6NT, UK

¹⁷ Department of Physics, The Ohio State University, 191 West Woodruff Avenue, Columbus, OH 43210, USA

¹⁸ Center for Computational Astrophysics, Flatiron Institute, New York, NY, USA

¹⁹ Virtual Planetary Laboratory, University of Washington, Seattle, WA, USA

²⁰ Institute for Astronomy, University of Hawai'i, 2680 Woodlawn Drive, Honolulu, HI 96822, USA

Received 2020 July 1; revised 2020 September 25; accepted 2020 September 28; published 2020 December 1

Abstract

Studies of Galactic structure and evolution have benefited enormously from Gaia kinematic information, though additional, intrinsic stellar parameters like age are required to best constrain Galactic models. Asteroseismology is the most precise method of providing such information for field star populations en masse, but existing samples for the most part have been limited to a few narrow fields of view by the CoRoT and Kepler missions. In an effort to provide well-characterized stellar parameters across a wide range in Galactic position, we present the second data release of red giant asteroseismic parameters for the K2 Galactic Archaeology Program (GAP). We provide ν_{\max} and $\Delta\nu$ based on six independent pipeline analyses; first-ascent red giant branch (RGB) and red clump (RC) evolutionary state classifications from machine learning; and ready-to-use radius and mass coefficients, κ_R and κ_M , which, when appropriately multiplied by a solar-scaled effective temperature factor, yield physical stellar radii and masses. In total, we report 4395 radius and mass coefficients, with typical uncertainties of 3.3% (stat.) $\pm 1\%$ (syst.) for κ_R and 7.7% (stat.) $\pm 2\%$ (syst.) for κ_M among RGB stars, and 5.0% (stat.) $\pm 1\%$ (syst.) for κ_R and 10.5% (stat.) $\pm 2\%$ (syst.) for κ_M among RC stars. We verify that the sample is nearly complete—except for a dearth of stars with $\nu_{\max} \lesssim 10\text{--}20 \mu\text{Hz}$ —by comparing to Galactic models and visual inspection. Our asteroseismic radii agree with radii derived from Gaia Data Release 2 parallaxes to within $2.2\% \pm 0.3\%$ for RGB stars and $2.0\% \pm 0.6\%$ for RC stars.

Unified Astronomy Thesaurus concepts: Asteroseismology (73); Catalogs (205); Stellar radii (1626); Stellar masses (1614); Red giant clump (1370); Red giant branch (1368)

Supporting material: machine-readable tables

1. Introduction

The Galactic Archaeology Program (GAP; Stello et al. 2015) has taken advantage of the multidirectional view of the Galaxy offered by the repurposed Kepler mission, K2. With hundreds of thousands of stars observed, K2's potential for studying the Galaxy is significant. Instead of a single snapshot of the Galaxy with Kepler (Borucki et al. 2008), K2 (Howell et al. 2014) observed along the ecliptic, including the local disk, the bulge, and even distant regions of the halo. Importantly for this work, the K2 mission has delivered the quality of data necessary for asteroseismic analysis.

The K2 GAP aims to provide fundamental stellar parameters for red giants across the Galaxy. In combination with temperature

and metallicity information, asteroseismology can provide stellar radii, masses, and when combined with stellar models, ages. Kepler red giant asteroseismology has yielded important findings for Galactic archeology, including verifying the presence of a vertical age gradient in the Galactic disk (Miglio et al. 2013; Casagrande et al. 2016), testing Galactic chemical evolution models (e.g., Spitoni et al. 2020), and confirming an age difference between chemically and kinematically defined thin and thick discs (Silva Aguirre et al. 2018). Nevertheless, the Kepler asteroseismic sample was not curated for Galactic studies, and so GAP's deliberate and well-understood target selection for Galactic archeology purposes sets up K2 to be a more useful tool

for Galactic archeology, particularly in light of its expanded view of the Galaxy. Indeed, the K2 data is providing interesting insights into the relative ages of chemically defined stellar populations beyond the solar vicinity (Rendle et al. 2019; J. T. Warfield et al. 2020, in preparation).

K2’s potential is tempered, however, by a decreased photometric precision compared to Kepler and an ~ 80 day dwell time per campaign instead of up to ~ 4 yr for Kepler. These two limitations mean that K2 is mostly suited for giants with $\log g$ above ~ 1.4 , probes one to two magnitudes “shallower” than Kepler, and yields less precise asteroseismic measurements compared to Kepler (Stello et al. 2017). Furthermore, although the accuracy of stellar parameters derived through asteroseismology is at the percent level (e.g., Huber et al. 2012; Silva Aguirre et al. 2012; Zinn et al. 2019b), at this level, there are measurement systematics that need to be corrected for (Pinsonneault et al. 2018). We therefore devote special attention in what follows to understanding the statistical and systematic uncertainties in our asteroseismic quantities.

We have previously released a collection of ν_{\max} and $\Delta\nu$ values for 1210 K2 GAP red giants in Stello et al. (2017). The present release covers campaigns 4, 6, and 7, and comprises 4395 stars. In addition to the global asteroseismic parameters, ν_{\max} and $\Delta\nu$, we also provide scaling-relation quantities that, when combined with an effective temperature, yield radii and masses. We also provide estimates of systematic and statistical errors on the asteroseismic quantities, and establish the completeness of observed targets in order to ensure a well-defined selection function.

2. Data

2.1. Target Selection

In the context of the GAP, analyses of the campaigns presented here were prioritized due to their coverage of the sky: the Galactic center (C7), the Galactic anticenter (C4), and out of the Galactic plane (C6). These results will ultimately be joined with a forthcoming analysis of the rest of the K2 campaigns for which GAP targets have been observed. The GAP targets red giants because they are bright (probing far into the Galaxy) and because their oscillations are detectable from the K2 long-cadence data, which has a Nyquist frequency of $\sim 280 \mu\text{Hz}$. All GAP targets for campaigns 4, 6, and 7 were selected from the Two Micron All Sky Survey (2MASS; Skrutskie et al. 2006) to have $J - K > 0.5$ and good photometric quality based on 2MASS flags.²¹ The proposed targets passing these selection criteria were prioritized based on a rank ordering in V -band magnitude from bright to faint.²² C4 and C6 targets were chosen to have $9 < V < 15$, and C7 targets were chosen to have $9 < V < 14.5$, with some exceptions to the prioritization on a campaign-to-campaign basis, as follows: One giant with existing RAVE data was prioritized in C4. In C6, priority was given to 129 giants with existing

²¹ The 2MASS `qflag` photometric quality flag was required to be *A* or *B* for *J*, *H*, and *K_s*, which ensures, among other things, that the signal-to-noise ratio is greater than 7. Additional flags ensured that the photometry did not suffer from confusion from nearby objects (`cflag` == 0); was a single, unblended source (`bflag` == 1); was not extended (`xflag` == 0); was not a known solar system object (`aflag` == 0); and had no neighbors within $6''$ (`prox` > 6.0). See <http://vizier.u-strasbg.fr/cgi-bin/VizieR?-source=B2mass> for more details.

²² At the time of targeting, it was typically not well-known which stars were giants or dwarfs, but generally the giant fraction was expected to be close to 100% at the bright end and down to as low as 20%, depending on the campaign, at the faint end of the selection.

Table 1
Targeted and Observed Stars as a Function of Campaign

Campaign	K2 GAP Targeted	K2 GAP Observed	GAP Selected Observed
C4	17410	6357	5000
C6	8371	8313	8300
C7	18698	4362	3500

Notes. “K2 GAP targeted” refers to the number of proposed targets and “K2 GAP observed” are those that were observed, including targets not following the GAP selection function (see text). “GAP selected observed” refers to the approximate number of GAP observed stars that follow the GAP target selection function from the bright end of $V = 9$ to a limiting magnitude of 13.447, 15, and 14.5 for C4, C6, and C7, respectively.

APOGEE (Majewski et al. 2010) spectra, 607 with existing RAVE spectra, and 5 low-metallicity giants chosen from the literature to be giants with $[\text{Fe}/\text{H}] < -3$. The highest priority for GAP targets in C7 was given to 222 known giants with existing spectroscopic data from APOGEE, and 23 targets in NGC 6717 (but see below).

Because observed targets were selected in a linear way from the target priority list, the selection functions for each of the campaigns are well-defined. Nearly all of the C6 targets were observed, and so the observed targets conform to the selection function $9 < V < 15$. Our C4 targets were observed down to $V = 13.447$, and therefore follow the selection function down to that magnitude limit (this magnitude limit approximately corresponds to the top 5000 GAP targets). In addition to these GAP-selected targets, there are fainter stars on the GAP target list that were serendipitously observed by K2 through other non-GAP target proposals. Those stars do not follow the GAP selection function but are still analyzed in this paper. However, we caution their use for population studies. The observed C7 targets were accidentally chosen from an inverted priority list during the mission-wide target list consolidation before upload to the spacecraft. As a result, observations were made of only two of the higher-priority APOGEE C7 targets and none from NGC 6717. As discussed in Sharma et al. (2019), the resulting effective selection function is one of either $9 < V < 14.5$ or $14.276 < V < 14.5$, depending on the position on the sky. Approximately, the 3500 lowest-priority GAP targets follow the full selection function. There is, however, an additional population of ~ 600 stars in C7 that can be used for scientific purposes, with the understanding that its selection function of $14.276 < V < 14.5$ is different than that of the rest of the campaign ($9 < V < 14.5$). For additional details, see Sharma et al. (2019). We account for these selection functions when comparing to models in our analysis by making sure to compare to the subset of observed stars that follow reproducible GAP target criteria. An accounting of observed and targeted stars is given in Table 1. The approximate lines of sight for these campaigns are shown in Figure 1. An on-sky map of the campaigns is shown in Figure 2.

2.2. K2 Light Curve Preprocessing

We used the light curves generated by the EVEREST pipeline (Luger et al. 2018), which uses campaign-specific basis vectors to remove noise correlated across pixels. Though the K2 GAP DR1 (Stello et al. 2017) used Vanderburg & Johnson (2014) (K2SFF) light curves, we found that the EVEREST pipeline removes at least as much of the sawtooth-like systematic flux

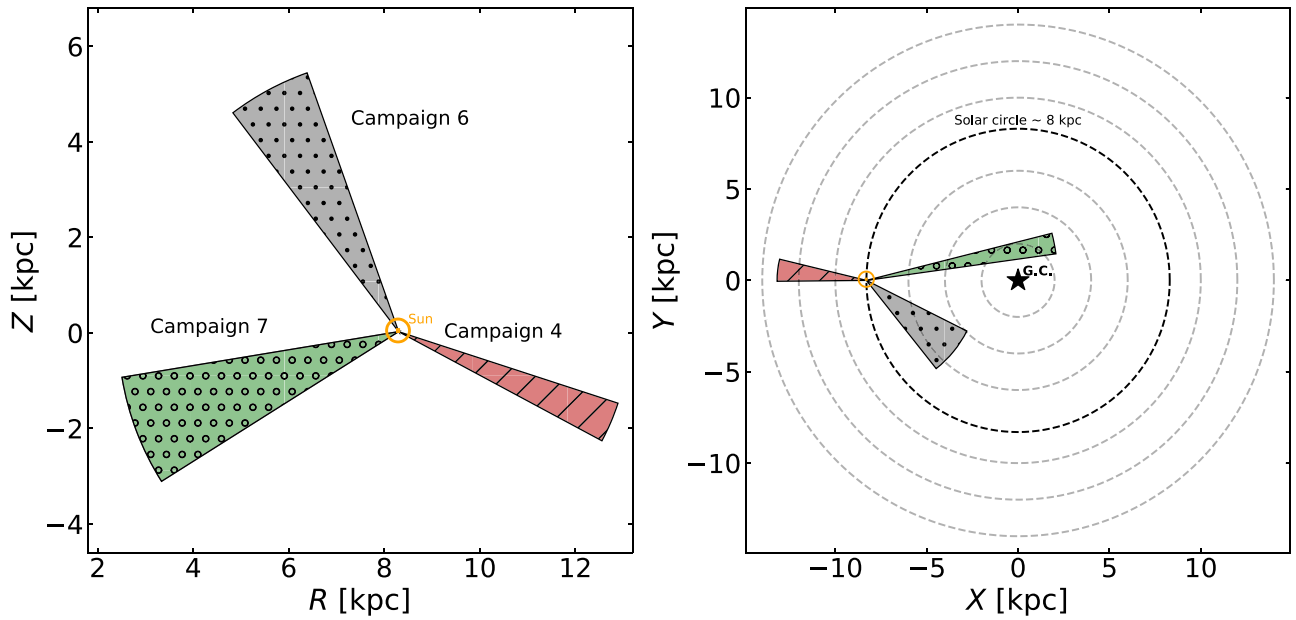


Figure 1. Left: approximate Z - R distribution of stars in K2 GAP DR2, for each campaign. Right: approximate X - Y distribution of stars in K2 GAP DR2, for each campaign.

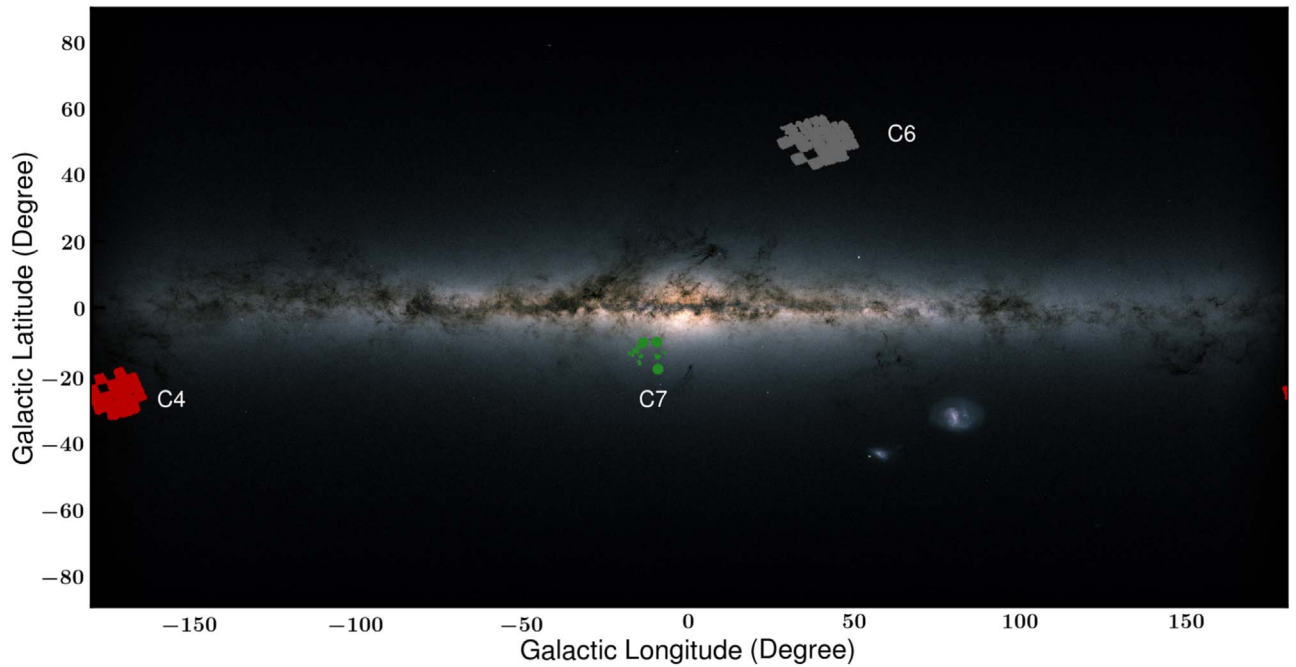


Figure 2. Positions of observed K2 GAP stars in C4, C6, and C7, relative to the Galactic plane. Background image modified from ESA/Gaia/DPAC.

variation induced by the K2 six-hour thruster firings as K2SFF does, while furthermore generating lower levels of white noise in the giant spectra than K2SFF. Because the K2 GAP DR1 used K2SFF light curves, we attempted to reconcile systematic differences in the amplitudes of flux variations in the EVEREST and K2SFF light curves for consistency between this release and DR1. To do so, for each star, we multiplied the EVEREST light-curve flux by a scalar factor such that its power is equal to the K2SFF power. We then applied a boxcar high-pass filter with a width of 4 days to the light curve to remove most of the non-oscillation variability (Stello et al. 2015), and 4σ outliers in the time series were removed. Seven targets were labeled as

extended in the EPIC and were not included in the present analysis.²³

3. Methods

3.1. Extraction of Asteroseismic Parameters

In this data release, we focus on two asteroseismic quantities, ν_{\max} and $\Delta\nu$, which we describe in turn.

²³ The following EPIC IDs are affected in C4: 210344244, 210489346, 210766860, 210497173, 210608879; and in C6: 212680904, 212708542.

The frequency at maximum acoustic power, ν_{\max} , scales with the acoustic cutoff frequency at the stellar atmosphere (Brown et al. 1991; Kjeldsen & Bedding 1995; Chaplin et al. 2008; Belkacem et al. 2011), such that

$$\frac{\nu_{\max}}{\nu_{\max,\odot}} \approx \frac{M/M_{\odot}}{(R/R_{\odot})^2 \sqrt{(T_{\text{eff}}/T_{\text{eff},\odot})}}. \quad (1)$$

The frequency separation between modes of the same degree but consecutive radial order, $\Delta\nu$, scales with the stellar density (Ulrich 1986; Kjeldsen & Bedding 1995) according to

$$\frac{\Delta\nu}{\Delta\nu_{\odot}} \approx \sqrt{\frac{M/M_{\odot}}{(R/R_{\odot})^3}}. \quad (2)$$

The $\nu_{\max,\odot}$ and $\Delta\nu_{\odot}$ solar reference values are not set in stone, and are themselves measured quantities from asteroseismic data of the Sun. All the pipelines have an internal set of recommended solar reference values, $\nu_{\max,\odot,\text{PIP}}$ and $\Delta\nu_{\odot,\text{PIP}}$. In addition to those pipeline-specific solar reference values, we adopt a solar reference temperature of $T_{\text{eff},\odot} = 5772$ K (Mamajek et al. 2015).

Like Stello et al. (2017), we analyze the data using multiple asteroseismic pipelines, descriptions of which are found therein. We briefly revisit each pipeline below.

A2Z+ (hereafter A2Z) is based on the A2Z pipeline described in Mathur et al. (2010). Two models are used to compute $\Delta\nu$: the autocorrelation function of the time series and the power spectrum of the power spectrum. The results from both methods are then compared, and a $\Delta\nu$ value is only kept when both methods agree to within 10%. The power density spectra (PDS) of those stars are checked to select the ones where modes are present to high confidence. The FLiPer metric (Bugnet et al. 2018) is used to check stars where the amplitude of the convective background does not agree with the seismic detection. Finally, the $\Delta\nu$ value is refined by cross-correlating a template of the radial modes around the region of the modes where $\Delta\nu$ is varied. The value reported corresponds to the one obtained for the highest correlation coefficient. After fitting the convective background with two Harvey laws (Mathur et al. 2011; Kallinger et al. 2014) and subtracting it from the PDS, a Gaussian function is fit to the modes in order to estimate the frequency of maximum power, ν_{\max} .

BHM (Elsworth et al. 2020) is based on the OCT pipeline (Hekker et al. 2010), and performs hypothesis testing for solar-like oscillations above the granulation background. If there is a frequency window that has significant signal, ν_{\max} and $\Delta\nu$ are computed according to Hekker et al. (2010), with increased, K2-specific quality control to ensure $\Delta\nu$ is not an alias of the true value.

CAN returns ν_{\max} and $\Delta\nu$ for stars whose autocorrelation functions have characteristic timescales and rms variability that accord with a relation expected from solar-like oscillators (Kallinger et al. 2016). A Bayesian evidence is computed to determine whether there are solar-like oscillations near the detected autocorrelation timescale (and therefore near ν_{\max}). A threshold for the evidence is determined based on visual inspection of a test set of power spectra. The value of $\Delta\nu$ is then calculated by fitting individual radial modes.

COR first fits for $\Delta\nu$ using the autocorrelation of the light curve. COR (Mosser & Appourchaux 2009) returns results for stars that have $\Delta\nu$, FWHM, amplitude of power, and the granulation at ν_{\max} that follow relations from Mosser et al. (2010), with stricter, K2-specific requirements for stars with a

possible ν_{\max} detected near the K2 thruster firing frequency (or alias thereof).

SYD computes ν_{\max} and $\Delta\nu$ according to Huber et al. (2009). Results are returned only for stars that are classified as having solar-like oscillations by a machine-learning algorithm described in Hon et al. (2018b). Results for $\Delta\nu$ are provided only for stars that are classified as having reliable $\Delta\nu$ values by a machine-learning algorithm. The $\Delta\nu$ -vetting algorithm is a convolutional neural network trained on K2 C1 data that were classified by eye as having detectable $\Delta\nu$ values. The algorithm takes as an input the autocorrelation of a granulation background-corrected spectrum in a window with a width of $\pm 0.59 \times \nu_{\max}^{0.9}$ centered around ν_{\max} . This latter window size is taken from the observed width of detected stellar oscillations in giants (Mosser et al. 2010). The algorithm takes the autocorrelation, passes it through a convolutional neural network, and outputs a score varying from 0 (not a valid $\Delta\nu$ detection) to 1 (100% certain valid $\Delta\nu$ detection), but which is not a linear mapping to percent confidence in the detection. For this reason, the score was calibrated using visually verified $\Delta\nu$ detections, which showed that a score of 0.8 corresponds to a completeness of about 70% (i.e., this score rejects 30% stars that have valid $\Delta\nu$ detections) and near total purity (i.e., all stars have visually verified $\Delta\nu$ detections); $\Delta\nu$ detections were considered valid for stars with a score above this 0.8 value.

BAM calculates ν_{\max} and $\Delta\nu$ according to Zinn et al. (2019c). The $\Delta\nu$ values for this data release are provided based on the autocorrelation method described therein, which, in turn, is based on that of SYD. Stars are classified as oscillators or not based on the Bayesian evidence for the presence of solar-like oscillations (for details, see Zinn et al. (2019c)), and results in this data release are returned for stars with $3.5 \mu\text{Hz} < \nu_{\max} < 250 \mu\text{Hz}$. Values of $\Delta\nu$ are only provided for those that satisfy the SYD $\Delta\nu$ -vetting algorithm described above.

Any pipeline may return a ν_{\max} and/or a $\Delta\nu$ for a given star. In what follows, however, we consider a “detection” for a given pipeline to be a target for which a ν_{\max} is returned, unless otherwise noted. A fraction of ν_{\max} -detected stars will not have a reliable $\Delta\nu$ measurement reported. The raw ν_{\max} and $\Delta\nu$ and the uncertainties reported by each pipeline are provided in Table 2, while the number of ν_{\max} and $\Delta\nu$ values returned are provided in Table 3.

3.2. Derived Quantities

3.2.1. Mean Asteroseismic Parameters, $\langle \nu'_{\max} \rangle$ and $\langle \Delta\nu' \rangle$

Consolidating results from multiple pipelines, as we do here, has three primary benefits: outliers can be rejected (e.g., stars that only one pipeline identifies as an oscillator can be considered dubious); the accuracy and precision of the parameters can be improved by averaging results for the same star from different pipelines; and the spread in values for a given star can be translated into an uncertainty estimate. To perform this averaging, however, the possibility that there are systematic differences in pipeline results needs to be taken into account. Pinsonneault et al. (2018) demonstrated that such systematics existed in their multipipeline analysis of Kepler data, finding that the relative zero points of the measurements returned by different pipelines do not scale in the same way as their solar measurements do (Pinsonneault et al. 2018). Figures 3 and 4 demonstrate these systematics in our K2 ν_{\max} and $\Delta\nu$ values. In what follows, we describe an approach that

Table 2
Raw Asteroseismic ν_{\max} and $\Delta\nu$ Values for K2 GAP DR2 for Each Pipeline, with Evolutionary States

EPIC	Campaign	Priority	Evo. State	$\nu_{\max,A2Z}$ (μHz)	$\sigma_{\nu_{\max,A2Z}}$ (μHz)	$\Delta\nu_{A2Z}$ (μHz)	$\sigma_{\Delta\nu_{A2Z}}$ (μHz)	$\nu_{\max,BAM}$ (μHz)	$\sigma_{\nu_{\max,BAM}}$ (μHz)	$\Delta\nu_{BAM}$ (μHz)	$\sigma_{\Delta\nu_{BAM}}$ (μHz)	$\nu_{\max,BHM}$ (μHz)	$\sigma_{\nu_{\max,BHM}}$ (μHz)	$\Delta\nu_{BHM}$ (μHz)
210306475	4	903	RGB	28.550	2.25	3.620	0.010	30.135	0.808	3.277	0.197	26.900	1.4	3.470
210307958	4	2771	RGB	27.940	2.47	3.890	0.000	30.316	0.723	3.723	0.124
210314854	4	1141	RGB	29.030	2.03	4.100	0.120	31.863	0.743	4.115	0.083	31.200	1.0	4.090
210315825	4	1651	RGB	59.580	3.63	5.910	0.160	59.253	1.379	5.899	0.060	60.000	1.3	6.010
210318976	4	988	RGB	24.800	1.88	3.270	0.040	25.080	0.841	21.700	1.1	3.080
$\sigma_{\Delta\nu,BHM}$ (μHz)	$\nu_{\max,CAN}$ (μHz)	$\sigma_{\nu_{\max,CAN}}$ (μHz)	$\Delta\nu_{CAN}$ (μHz)	$\sigma_{\Delta\nu,CAN}$ (μHz)	$\nu_{\max,COR}$ (μHz)	$\sigma_{\nu_{\max,COR}}$ (μHz)	$\Delta\nu_{COR}$ (μHz)	$\sigma_{\Delta\nu,COR}$ (μHz)	$\nu_{\max,SYD}$ (μHz)	$\sigma_{\nu_{\max,SYD}}$ (μHz)	$\Delta\nu_{SYD}$ (μHz)	$\sigma_{\Delta\nu,SYD}$ (μHz)		
0.160	27.670	1.27	29.016	0.63245	3.450	0.170		
...	29.260	1.03	4.004	0.094	28.350	0.83	3.805	0.083	28.789	0.62378	3.740	0.203		
0.190	30.600	1.49	4.066	0.056	31.640	0.89	4.204	0.079	31.044	0.88666	4.033	0.238		
0.190	59.390	1.28	5.960	0.084	58.960	1.26	5.975	0.087	59.213	1.21725	5.873	0.058		
0.100	23.660	1.22	3.482	0.090	24.540	0.73	3.402	0.076	24.144	0.77871		

Notes. These are the parameters returned by a given pipeline, along with their uncertainties, without any of the rescaling described in Section 3.2.1 applied. Evolutionary states, which have been derived in this work (see Section 3.2.2), are also included in this table. If classified, a star's evolutionary state is assigned as either "RGB," "RGB/AGB," or "RC." "Priority" refers to the K2 GAP target priority discussed in Section 2 (a smaller numerical value corresponds to higher priority); serendipitous targets do not have a populated priority entry.

(This table is available in its entirety in machine-readable form.)

Table 3
Asteroseismic Yields across Pipeline and Campaign

		ν_{\max}	ν'_{\max}	$\Delta\nu$	$\Delta\nu'$	κ'_R	κ'_M
C4	A2Z	1536	1375	1536	1331	1331	1331
C6	A2Z	1086	1018	1086	985	985	985
C7	A2Z	993	912	293	279	279	279
Total	A2Z	3615	3305	2915	2595	2595	2595
C4	BAM	2478	1480	844	741	741	741
C6	BAM	2529	1515	955	844	844	844
C7	BAM	2315	1267	677	589	589	589
Total	BAM	7322	4262	2476	2174	2174	2174
C4	BHM	1984	1414	1529	1189	1189	1189
C6	BHM	2275	1482	1702	1229	1229	1229
C7	BHM	1803	1231	1238	1019	1019	1019
Total	BHM	6062	4127	4469	3437	3437	3437
C4	CAN	1897	1395	968	788	788	788
C6	CAN	1956	1420	1455	1189	1189	1189
C7	CAN	1564	1137	1048	889	889	889
Total	CAN	5417	3952	3471	2866	2866	2866
C4	COR	1803	1374	1803	1304	1304	1304
C6	COR	1443	1118	1443	1043	1043	1043
C7	COR	1561	1188	1561	1149	1149	1149
Total	COR	4807	3680	4807	3496	3496	3496
C4	SYD	2136	1416	853	695	695	695
C6	SYD	2207	1335	868	727	727	727
C7	SYD	1675	1089	584	503	503	503
Total	SYD	6018	3840	2305	1925	1925	1925

Note. Numbers of stars with raw asteroseismic values (ν_{\max} , $\Delta\nu$), rescaled asteroseismic values (ν'_{\max} , $\Delta\nu'$), and radius and mass coefficients (κ'_R , κ'_M), as a function of pipeline and campaign.

rescales each pipeline's ν_{\max} and $\Delta\nu$ values such that they are on average on the same scale as the other pipelines. These rescaled values are used to perform outlier rejection with sigma clipping, and the values are averaged for each star in order to compute more accurate and precise asteroseismic values, as well as to define empirical uncertainties on ν_{\max} and $\Delta\nu$.

To reduce the systematic uncertainty across pipelines for a single star, we follow the approach taken by Pinsonneault et al. (2018): under the assumption that each pipeline's ν_{\max} and $\Delta\nu$ values are distributed around the true values, we can fit for near-unity scale factors that effectively modify each pipeline's solar reference values so that the mean ν_{\max} and $\Delta\nu$ returned by pipelines are all on the same scale. This therefore reduces the systematic uncertainty due to the choice of a single pipeline value on a single star's ν_{\max} or $\Delta\nu$, and it allows for averaging values across pipelines on a star-by-star basis.

The above procedure to rescale the pipeline-specific solar reference values is performed by initially assuming that the pipeline values are already on the same system, so that the rescaled ν_{\max} , $\nu'_{\max,s,p}$, of a star, s , for pipeline, p , equals the raw value returned by the pipeline: $\nu'_{\max,s,p} = \nu_{\max,s,p}$. An average value $\langle \nu'_{\max,s} \rangle \equiv \sum_p \nu'_{\max,s,p} / N_p$ is then calculated for each star that has at least two pipelines returning a value. The sum is over those N_p reporting pipelines. A scalar factor for each pipeline, $X_{\nu_{\max},p} \equiv \sum_s [\nu_{\max,s,p} / \langle \nu'_{\max,s} \rangle] / N_s$, is calculated using the N_s stars for which the pipeline returned a raw value, $\nu_{\max,s,p}$, and which had a defined mean value $\langle \nu'_{\max,s} \rangle$. The pipeline values are rescaled by this factor so that $\nu'_{\max,s,p} = \nu_{\max,s,p} / X_{\nu_{\max},p}$. For each star, a 3σ clipping is performed to reject rescaled values returned by a pipeline that are highly discordant with the results from other

pipelines. This whole process is repeated until convergence in the rescaled value, $\nu'_{\max,s,p}$. The same procedure is done for $\Delta\nu$. Following the observation by Pinsonneault et al. (2018) that the RC exhibits significantly different structure in the pipeline ν_{\max} and $\Delta\nu$ zero-point differences, the same procedure is done separately for RGB and RGB/AGB stars and RC stars. In the end, four scale factors are derived for each pipeline: a ν_{\max} scale factor for RGB stars, a $\Delta\nu$ scale factor for RGB stars, a ν_{\max} scale factor for RC stars, and a $\Delta\nu$ scale factor for RC stars. The resulting factors are at the percent level or below. For each pipeline, we provide the rescaled values, ν'_{\max} and $\Delta\nu'$, in addition to the raw values. We also provide mean values $\langle \nu'_{\max} \rangle$ and $\langle \Delta\nu' \rangle$, which have been averaged across pipelines. The root mean squares across all pipelines for each star are taken as the uncertainties on the $\langle \nu'_{\max} \rangle$ and $\langle \Delta\nu' \rangle$ values, $\sigma_{\langle \nu'_{\max} \rangle}$ and $\sigma_{\langle \Delta\nu' \rangle}$ (see Section 3.2.3). The sample with $\langle \nu'_{\max} \rangle$ is shown in Figure 5.

Unless otherwise noted, the mean $\Delta\nu$ values for each star, $\langle \Delta\nu' \rangle$, as well as the pipeline-specific rescaled $\Delta\nu$ values, $\Delta\nu'$, have been multiplied by a factor as described in Sharma et al. (2016) that depends on the star's temperature, metallicity, surface gravity, mass, and evolutionary state. This factor is provided in Table 4 as X_{Sharma} , and is a theoretically motivated factor that improves the homology assumption in the $\Delta\nu$ scaling relation (Equation (2)). We calculated these factors using temperatures and metallicities from the EPIC (Huber et al. 2016); surface gravities from Equation (1) using ν_{\max} ; mass estimates from Equation (6) using ν_{\max} and $\Delta\nu$, before the factor in question has been applied; and evolutionary states derived from the neural network approach laid out in Section 3.2.2. The correction is applied multiplicatively such that $\Delta\nu'$ is multiplied by X_{Sharma} . Pipeline values rejected by the above sigma-clipping process will not have a corrected pipeline value populated in Table 4.

Table 5 shows the resulting solar reference scale factors compared to those from Pinsonneault et al. (2018). The agreement is mixed, depending on the pipeline. As noted in Section 3.1, the pipelines as implemented for this analysis have been modified to account for K2 data, and so may well differ slightly in the way they perform compared to their implementation for Pinsonneault et al. (2018). Additionally, we consider results from BAM (Zinn et al. 2019c), which the Pinsonneault et al. (2018) analysis did not consider. The uncertainties on the scale factors derived in this work are also larger than the ones found by Pinsonneault et al. (2018), in part due to the increased scatter in the ν_{\max} and $\Delta\nu$ derived with K2 data compared to Kepler data. These uncertainties are calculated assuming $\sigma_{\nu_{\max}}$ and $\sigma_{\Delta\nu}$ are exact (i.e., with no uncertainty on the standard deviation used to calculate them (see Section 3.2.3)). Given this assumption, the uncertainties on the scale factors are indicative and not definitive. We also provide the rescaled, pipeline-specific solar reference values themselves in Table 5 (attained by multiplying the pipeline-specific solar reference value by the pipeline's solar reference scale factor derived here).

Even with these rescalings, residual differences between pipelines as a function of ν_{\max} and $\Delta\nu$ will remain. These trends are shown in the bottom panels of Figures 6–9, where fractional differences between $\langle \nu'_{\max} \rangle$ and $\langle \Delta\nu' \rangle$ and individual pipeline rescaled values, ν'_{\max} and $\Delta\nu'$ are shown. By definition, the means of ν'_{\max} and $\Delta\nu'$ across the pipelines are $\langle \nu'_{\max} \rangle$ and $\langle \Delta\nu' \rangle$, though what these figures demonstrate is substructure as a function of ν_{\max} and $\Delta\nu$, indicating ν_{\max} - and $\Delta\nu$ -dependent

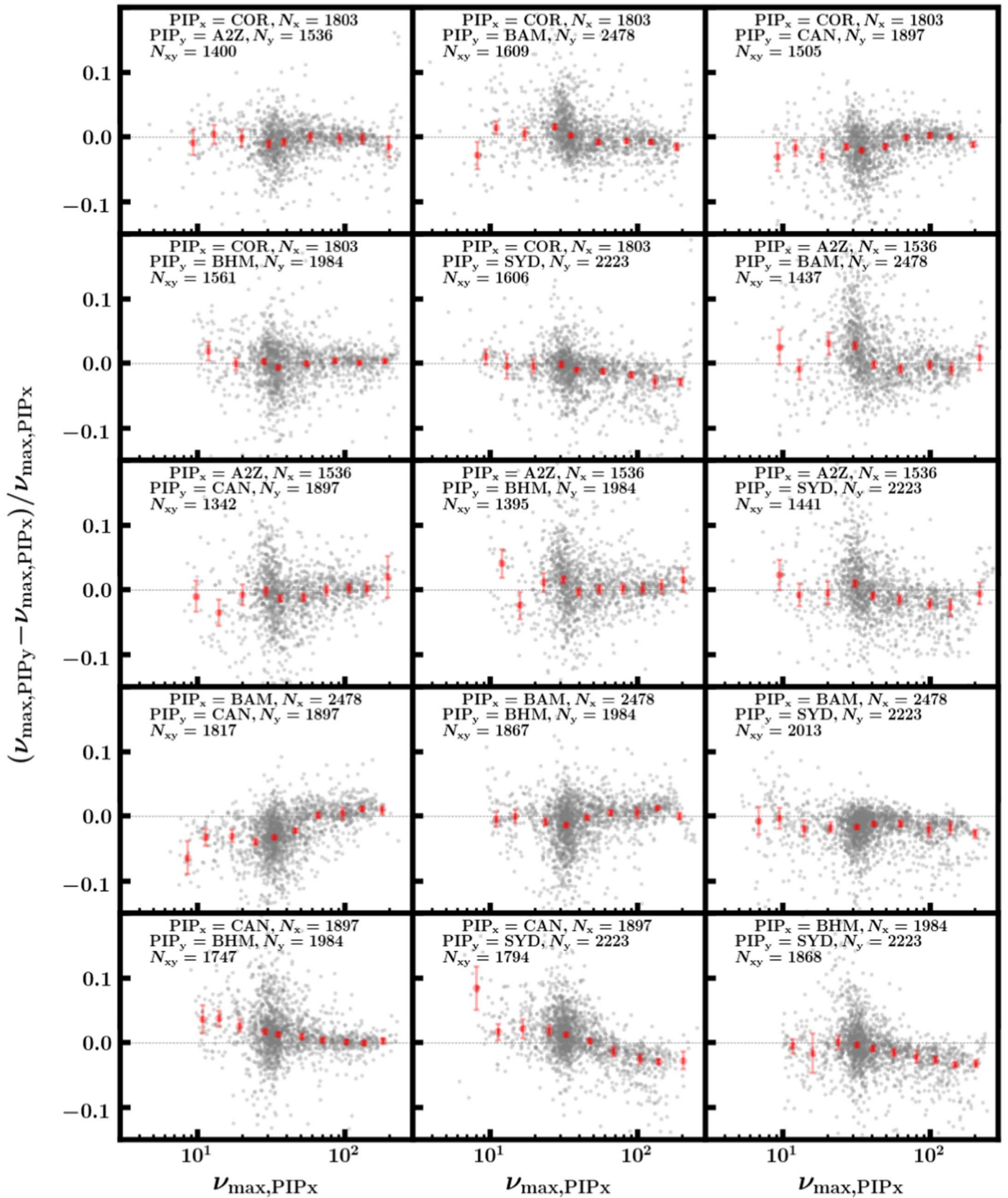
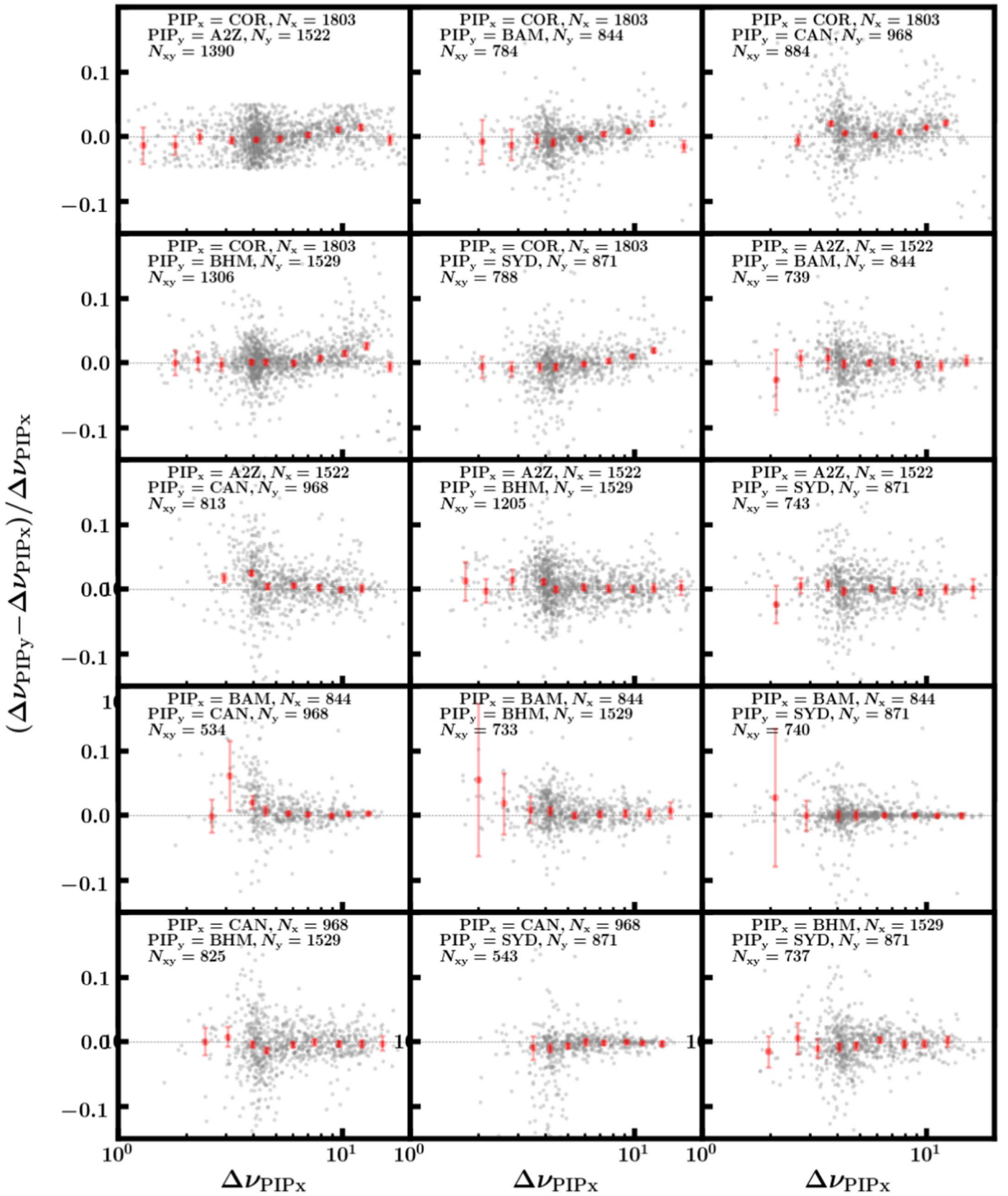


Figure 3. Pairwise comparisons between asteroseismology pipeline ν_{\max} values for K2 C4. Red error bars represent binned medians and uncertainties on those binned medians. N_x and N_y indicate the number of stars with nonzero asteroseismic values and uncertainties returned for pipeline x and pipeline y , with the number of stars returned by both pipelines indicated by N_{xy} . Trends seen here are present in C6 and C7 as well.

Figure 4. Same as Figure 3, but for $\Delta\nu$.

systematic errors, not zero-point errors. We turn to a more robust estimate of the systematic errors on $\langle\nu'_{\max}\rangle$ and $\langle\Delta\nu'\rangle$ in Section 4.2.

After these rescalings are applied for each pipeline ν_{\max} and $\Delta\nu$, the absolute value of the solar reference values are free to be chosen, which we take to be $\nu_{\max,\odot} = 3076 \mu\text{Hz}$ and

Table 4
Derived Asteroseismic ν_{\max} and $\Delta\nu$ Values for K2 GAP DR2

EPIC	$\langle\nu'_{\max}\rangle$ (μHz)	$\sigma_{\langle\nu'_{\max}\rangle}$ (μHz)	$N_{\nu_{\max}}$	$\langle\Delta\nu'\rangle$ (μHz)	$\sigma_{\langle\Delta\nu'\rangle}$ (μHz)	$N_{\Delta\nu}$	X_{Sharma}	$\sigma_{X_{\text{Sharma}}}$	$\langle\Delta\nu\rangle$ (μHz)	$\nu'_{\max,\text{A2Z}}$ (μHz)	$\Delta\nu'_{\text{A2Z}}$ (μHz)
210306475	28.487	1.235	5	3.610	0.099	3	1.027	0.010	3.517	28.502	3.723
210307958	28.974	0.935	5	3.957	0.123	5	1.032	0.013	3.834	27.893	4.090
210314854	30.907	0.990	6	4.170	0.057	6	1.016	0.018	4.102	28.981	4.167
210315825	59.422	0.463	6	6.088	0.045	6	1.025	0.010	5.939	59.479	6.071
210318976	24.478	0.414	5	3.487	0.094	3	1.031	0.013	3.381	24.758	3.381

$\nu'_{\max,\text{BAM}}$ (μHz)	$\Delta\nu'_{\text{BAM}}$ (μHz)	$\nu'_{\max,\text{BHM}}$ (μHz)	$\Delta\nu'_{\text{BHM}}$ (μHz)	$\nu'_{\max,\text{CAN}}$ (μHz)	$\Delta\nu'_{\text{CAN}}$ (μHz)	$\nu'_{\max,\text{COR}}$ (μHz)	$\Delta\nu'_{\text{COR}}$ (μHz)	$\nu'_{\max,\text{SYD}}$ (μHz)	$\Delta\nu'_{\text{SYD}}$ (μHz)	EPIC T_{eff} (K)	σ_T (K)	EPIC [Fe/H]	$\sigma_{[\text{Fe}/\text{H}]}$
30.004	...	26.764	3.558	27.948	29.218	3.547	4797	134	-0.27	0.30
30.184	3.853	29.554	4.110	28.249	3.926	28.990	3.867	4750	138	-0.36	0.26
31.724	4.202	31.042	4.157	30.907	4.118	31.527	4.268	31.260	4.115	4953	174	-0.51	0.33
58.995	6.067	59.696	6.156	59.986	6.077	58.749	6.125	59.626	6.029	4827	180	-0.30	0.30
24.971	23.897	3.565	24.452	3.508	24.312	...	4680	140	-0.20	0.26

Notes. Asteroseismic values rescaled for scalar offsets among pipelines are denoted by a prime (the pipeline-specific solar reference scale factors are listed in Table 5); mean ν_{\max} and $\Delta\nu$ values for each star across all pipelines are denoted by $\langle\nu'_{\max}\rangle$ and $\langle\Delta\nu'\rangle$; the standard deviation of these values for each star across all pipelines are denoted by $\sigma_{\langle\nu'_{\max}\rangle}$ and $\sigma_{\langle\Delta\nu'\rangle}$. The value of $\langle\Delta\nu'\rangle$ is adjusted using theoretically motivated correction factors, X_{Sharma} (Sharma et al. 2016), for use in asteroseismic scaling relations; an uncorrected version of $\langle\Delta\nu'\rangle$ for each star is provided, $\langle\Delta\nu\rangle = \langle\Delta\nu'\rangle/X_{\text{Sharma}}$, should the user wish to compute custom $\Delta\nu$ corrections. EPIC temperatures and metallicities are provided for this purpose, though these are relatively uncertain estimates of the true temperatures and metallicities (these uncertainties are also provided for convenience). The uncertainties in X_{Sharma} and $\sigma_{X_{\text{Sharma}}}$ are computed by perturbing the EPIC temperature and metallicities in a Monte Carlo procedure. Pipeline-specific rescaled values, ν'_{\max} and $\Delta\nu'$, are only provided for targets for which at least two pipelines returned concordant results, and otherwise have a blank entry; the numbers of pipelines returning valid results for ν_{\max} or $\Delta\nu$ are denoted by $N_{\nu_{\max}}$ and $N_{\Delta\nu}$. See text for details.

(This table is available in its entirety in machine-readable form.)

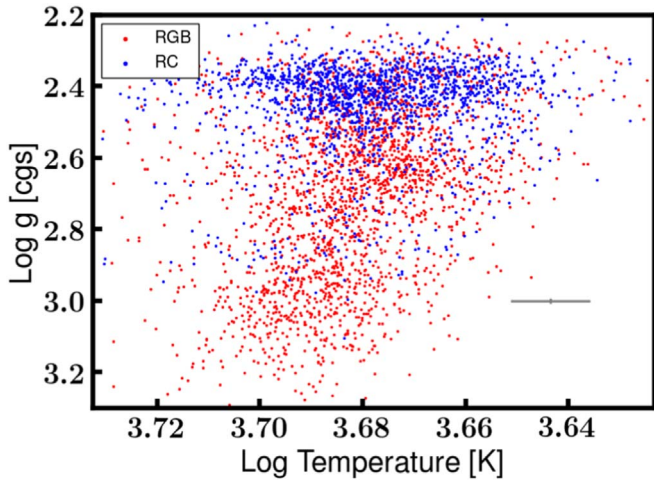


Figure 5. Kiel diagram for the C4-, C6-, and C7-observed K2 GAP DR2 stars, colored by evolutionary state, and using EPIC effective temperatures. A characteristic error bar is shown in the bottom right corner. Surface gravities are computed using $\langle\nu'_{\max}\rangle$, and so only stars with consensus values from multiple asteroseismic pipelines are shown.

$\Delta\nu_{\odot} = 135.146 \mu\text{Hz}$ (Pinsonneault et al. 2018). The effect of this choice is evaluated in Section 4.2.

The main K2 GAP DR2 sample is defined to be that with a valid $\langle\nu'_{\max}\rangle$ and $\langle\Delta\nu'\rangle$ (i.e., stars for which at least two pipelines returned both ν_{\max} and $\Delta\nu$ that agree to within 3σ), and its contents are summarized in Table 4. The sample contains 4395 stars.

3.2.2. Evolutionary States

Recent results have shown that highly accurate evolutionary state classification between RGB and RC can be achieved even

on short (K2-like) time series using machine-learning approaches (Hon et al. 2017, 2018a; Kuszlewicz et al. 2020) where “classical” asteroseismic-based classification is not possible (Bedding et al. 2011; Elsworth et al. 2019; Mosser et al. 2019). We note also that determining the evolutionary state for a short time series may be possible by measuring ϵ_c , the radial order position for the central radial mode of a power spectrum, to the extent that mode identification is possible with K2 light curves; see Kallinger et al. (2012). In this work, we determine evolutionary state using the method described in Hon et al. (2017, 2018a), which has an accuracy similar to that of the recent machine-learning approach from Kuszlewicz et al. (2020; 93% and 91% for K2-like data, respectively). The chosen technique requires that the granulation background of the stellar power spectrum be removed, and that ν_{\max} and $\Delta\nu$ be provided in order to search the appropriate part of the spectrum for evolutionary state diagnostics. We remove the background by subtracting a smoothed version of each power spectrum in log space. This approach avoids removing low-frequency modes, as can happen when smoothing with a window with fixed size in linear frequency, by using the fact that solar-like oscillators with different ν_{\max} have similar granulation background shapes in log space. We then apply the machine-learning technique from Hon et al. (2017, 2018a) using the background-subtracted power spectrum, $\langle\nu'_{\max}\rangle$, and $\langle\Delta\nu'\rangle$ as inputs. For details on how the neural network is trained, including how the probability of being RGB or RC is calibrated, see Hon et al. (2017, 2018a). Because the machine-learning algorithm was not trained on stars with $\Delta\nu < 3.2 \mu\text{Hz}$ (corresponding to stars with radii larger than those in the RC), we assign stars in this $\Delta\nu$ regime to be ambiguous RGB/AGB stars. The spectra of these stars from K2 cannot be used to distinguish between RGB and AGB because both types of stars are shell-burning stars, and so we consider them for the

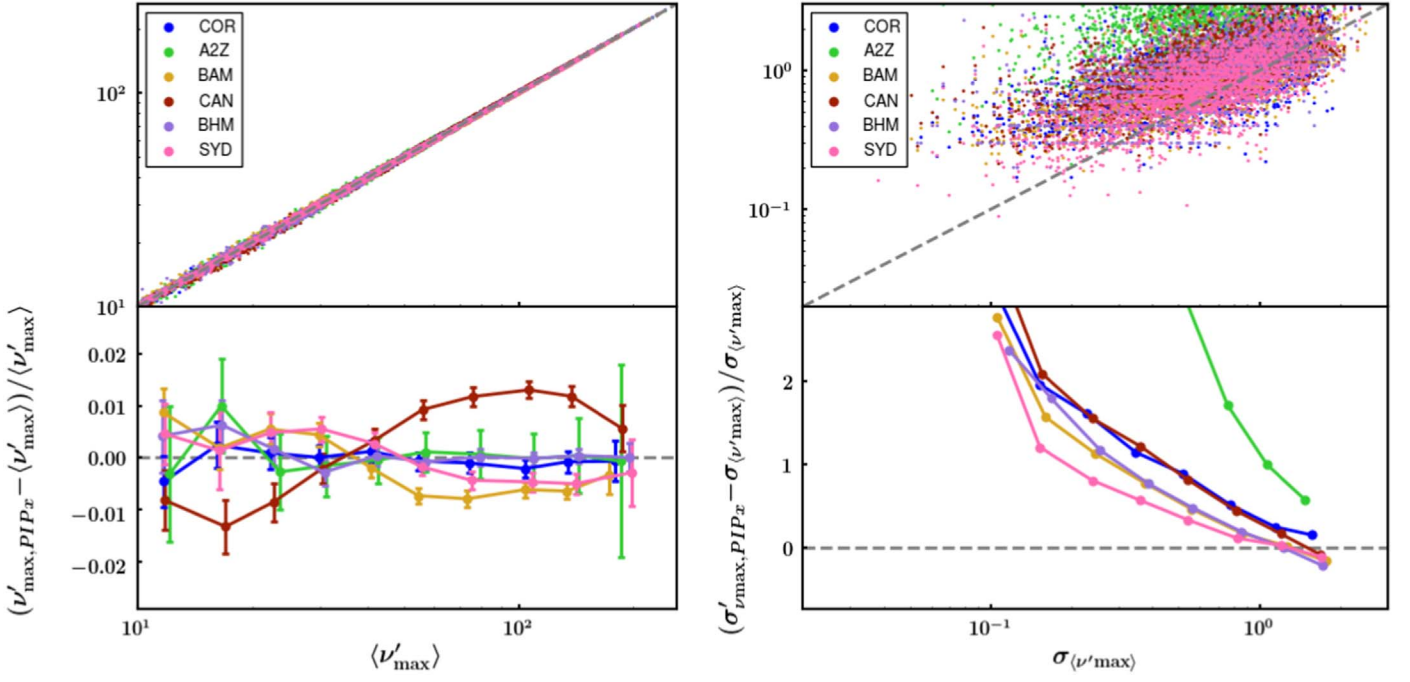


Figure 6. Left: comparison of RGB ν_{\max} among pipelines, showing the rescaled ν'_{\max} from each pipeline vs. the mean $\langle \nu'_{\max} \rangle$ across pipelines in the top panel, and the fractional difference between $\langle \nu'_{\max} \rangle$ and ν'_{\max} in the bottom panel, with error bars showing binned errors on the median fractional difference, assuming the uncertainty on $\langle \nu'_{\max} \rangle$ to be the standard deviation among the rescaled pipeline ν'_{\max} values, $\sigma_{\langle \nu'_{\max} \rangle}$ (this quantity is described in Sections 3.2.1 and 3.2.3). Right: $\sigma_{\nu'_{\max}}$ is plotted against the reported uncertainty on ν'_{\max} for each pipeline. Fractional differences between the two uncertainties are shown in the bottom panel.

Table 5
Derived Solar Reference Value Scale Factors and Solar Reference Values

	A2Z	CAN	COR	SYD	BAM	BHM
$X_{\nu_{\max}, \text{RGB}, \text{APOKASC2}}$	1.0023 ± 0.00002	1.0082 ± 0.00002	0.9989 ± 0.00002	1.0006 ± 0.00002
$X_{\nu_{\max}, \text{RGB}}$	1.0017 ± 0.00150	0.9901 ± 0.00072	1.0036 ± 0.00062	0.9931 ± 0.00072	1.0044 ± 0.00056	1.0051 ± 0.00063
$\nu_{\max, \odot \text{RGB}}$	3103 ± 5	3109 ± 2	3061 ± 2	3069 ± 2	3108 ± 2	3066 ± 2
$X_{\Delta\nu, \text{RGB}, \text{APOKASC2}}$	0.9993 ± 0.00001	1.0007 ± 0.00001	1.0051 ± 0.00001	0.9995 ± 0.00001
$X_{\Delta\nu, \text{RGB}}$	0.9977 ± 0.00090	1.0050 ± 0.00048	1.0001 ± 0.00061	0.9982 ± 0.00120	0.9966 ± 0.00159	1.0008 ± 0.00099
$\Delta\nu_{\odot \text{RGB}}$	134.6 ± 0.1	135.6 ± 0.1	134.9 ± 0.1	134.9 ± 0.2	134.4 ± 0.2	135.0 ± 0.1
$X_{\nu_{\max}, \text{RC}, \text{APOKASC2}}$	1.0035 ± 0.00003	1.0067 ± 0.00002	0.9909 ± 0.00002	1.0010 ± 0.00003
$X_{\nu_{\max}, \text{RC}}$	0.9931 ± 0.00260	0.9830 ± 0.00115	1.0056 ± 0.00090	0.9971 ± 0.00113	1.0160 ± 0.00083	0.9989 ± 0.00101
$\nu_{\max, \odot \text{RC}}$	3076 ± 8	3086 ± 4	3067 ± 3	3081 ± 3	3143 ± 3	3047 ± 3
$X_{\Delta\nu, \text{RC}, \text{APOKASC2}}$	0.9965 ± 0.00003	1.0108 ± 0.00002	0.9960 ± 0.00001	1.0032 ± 0.00002
$X_{\Delta\nu, \text{RC}}$	0.9960 ± 0.00151	1.0070 ± 0.00094	1.0006 ± 0.00086	0.9927 ± 0.00390	0.9945 ± 0.00328	1.0032 ± 0.00154
$\Delta\nu_{\odot \text{RC}}$	134.4 ± 0.2	135.9 ± 0.1	135.0 ± 0.1	134.1 ± 0.5	134.1 ± 0.4	135.3 ± 0.2

Note. Factors and values from this work (see Section 3.2.1), compared to those computed for some of the same pipelines using a similar method with Kepler data (Pinsonneault et al. 2018; ‘‘APOKASC-2’’).

purposes of the following analysis to be equivalent to RGB stars.

3.2.3. Uncertainties on $\langle \nu'_{\max} \rangle$ and $\langle \Delta\nu' \rangle$, $\sigma_{\nu'_{\max}}$, and $\sigma_{\langle \Delta\nu' \rangle}$

The root mean square of the rescaled ν'_{\max} and $\Delta\nu'$ values for each star across pipelines can be thought of as—and in this work are taken to be—the statistical uncertainties on $\langle \nu'_{\max} \rangle$ and $\langle \Delta\nu' \rangle$, denoted $\sigma_{\langle \nu'_{\max} \rangle}$ and $\sigma_{\langle \Delta\nu' \rangle}$. These values are listed in Table 4. We compare $\sigma_{\langle \nu'_{\max} \rangle}$ and $\sigma_{\langle \Delta\nu' \rangle}$ to the reported statistical uncertainties on the parameters returned by each pipeline in the bottom panels of Figures 6–9. These panels show the fractional differences in the pipeline-reported uncertainty and the root mean square of ν'_{\max}

and $\Delta\nu'$ across pipelines, and indicate whether or not the pipeline values are overestimated (above the gray dashed line) or underestimated (below the gray dashed line), assuming the pipeline values are distributed like normal variables around $\langle \nu'_{\max} \rangle$ and $\langle \Delta\nu' \rangle$. The uncertainties in ν_{\max} and $\Delta\nu$ appear to be overestimated for stars with smaller $\sigma_{\nu'_{\max}}$ and $\sigma_{\langle \Delta\nu' \rangle}$. This overestimation worsens with decreasing $\sigma_{\nu'_{\max}}$ and $\sigma_{\langle \Delta\nu' \rangle}$, and does so more rapidly for RC stars than RGB stars. Part of this overestimation trend may well be a selection effect: $\sigma_{\nu'_{\max}}$ and $\sigma_{\langle \Delta\nu' \rangle}$ are computed after a sigma-clipping procedure, which will tend to make a smaller root mean square. We evaluate the accuracy of these uncertainties further in Section 3.3.

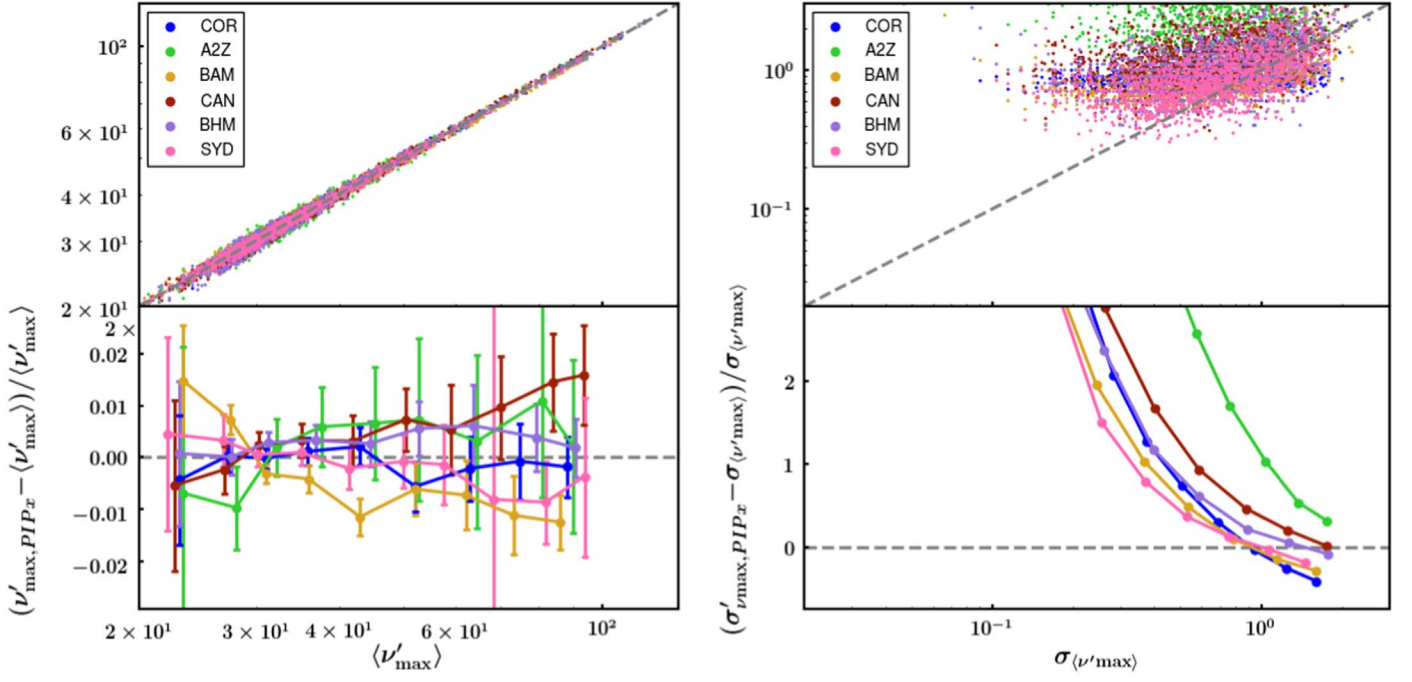
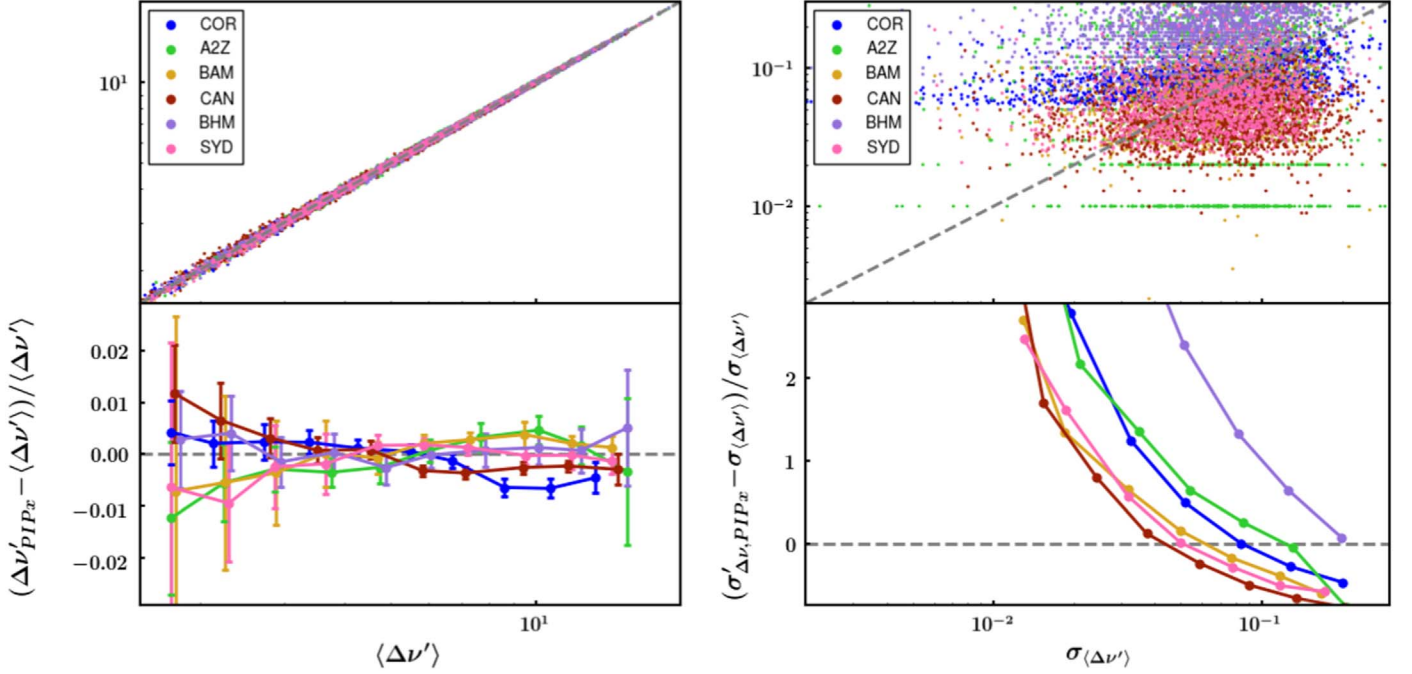


Figure 7. Same as Figure 6, but for RC stars.


 Figure 8. Same as Figure 6, but for $\Delta\nu$.

3.2.4. Radius and Mass Coefficients, $\langle\kappa'_R\rangle$ and $\langle\kappa'_M\rangle$

Given Equations (1) and (2), the radius of a star may be derived according to

$$\frac{R}{R_\odot} \approx \left(\frac{\nu_{\max}}{\nu_{\max,\odot}} \right) \left(\frac{\Delta\nu}{\Delta\nu_\odot} \right)^{-2} \left(\frac{T_{\text{eff}}}{T_{\text{eff},\odot}} \right)^{1/2} \quad (3)$$

$$\equiv \kappa_R \left(\frac{T_{\text{eff}}}{T_{\text{eff},\odot}} \right)^{1/2}, \quad (4)$$

and its mass according to

$$\frac{M}{M_\odot} \approx \left(\frac{\nu_{\max}}{\nu_{\max,\odot}} \right)^3 \left(\frac{\Delta\nu}{\Delta\nu_\odot} \right)^{-4} \left(\frac{T_{\text{eff}}}{T_{\text{eff},\odot}} \right)^{3/2} \quad (5)$$

$$\equiv \kappa_M \left(\frac{T_{\text{eff}}}{T_{\text{eff},\odot}} \right)^{3/2}. \quad (6)$$

It is our wish not to impose a choice of temperature on the user when providing asteroseismic radii and masses, which is why we provide κ_R and κ_M instead of direct radius and mass.

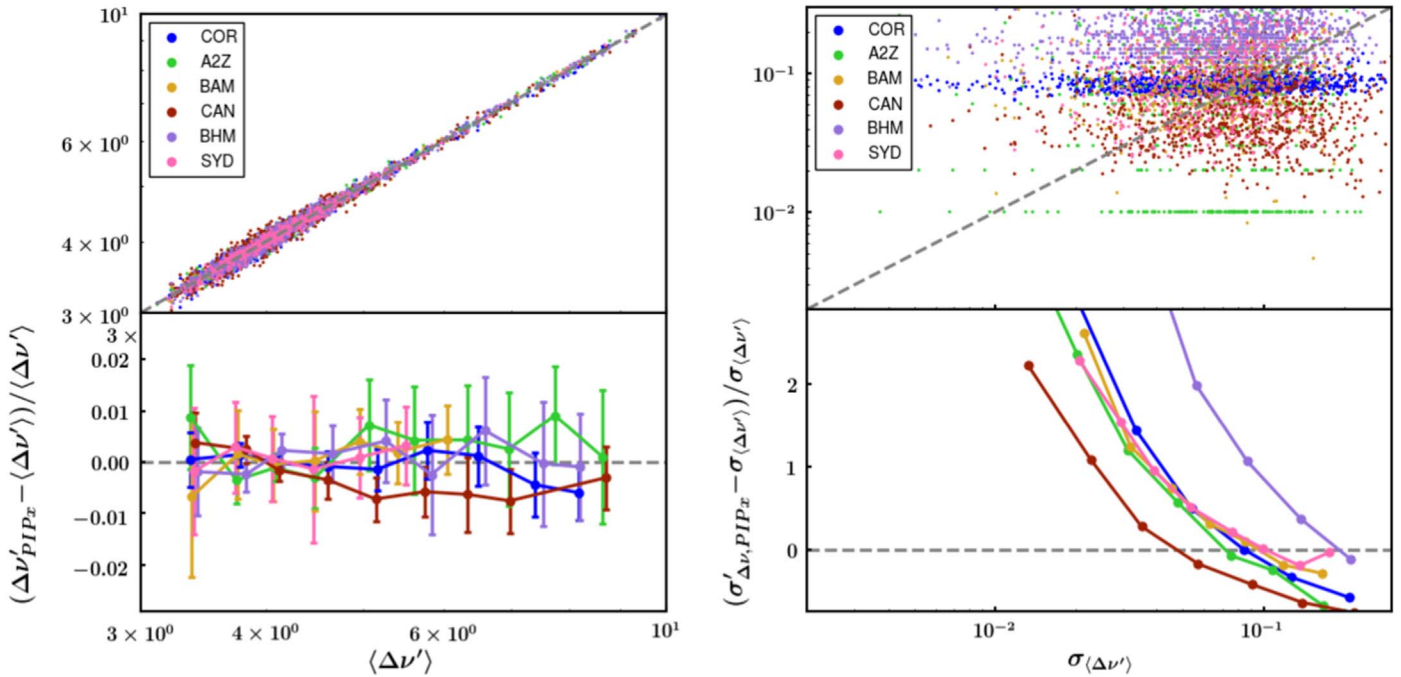


Figure 9. Same as Figure 8, but for RC stars.

With the rescaled asteroseismic values, ν'_{\max} and $\Delta\nu'$, in hand, we can construct the radius and mass coefficients, κ'_R and κ'_M , for each star and each pipeline, which correspond to the asteroseismic component of the scaling relations for stellar mass and radius in solar units. We show the pairwise comparisons between pipeline values of κ'_R and κ'_M for all stars in the DR2 sample in Figures 10 and 11. As with the pairwise ν_{\max} and $\Delta\nu$ comparisons (Figures 3 and 4), we see systematic differences between pipeline κ'_R and κ'_M values, which we quantify in Section 3.4. We also construct the average for each star, $\langle\kappa'_R\rangle$ and $\langle\kappa'_M\rangle$, based on $\langle\nu'_{\max}\rangle$ and $\langle\Delta\nu'\rangle$. Uncertainties on $\langle\kappa'_R\rangle$ and $\langle\kappa'_M\rangle$ are calculated according to standard propagation of error, using $\sigma_{\nu'_{\max}}$ and $\sigma_{\Delta\nu'}$. All of these coefficients are reported in Table 6.

3.3. Statistical Uncertainties in $\langle\nu'_{\max}\rangle$, $\langle\Delta\nu'\rangle$, $\langle\kappa'_R\rangle$, and $\langle\kappa'_M\rangle$

We show in Figures 20–21 the distribution of the fractional uncertainties, $\sigma_{\nu'_{\max}}/\langle\nu'_{\max}\rangle$ and $\sigma_{\Delta\nu'}/\langle\Delta\nu'\rangle$, as a function of evolutionary state (RGB or RGB/AGB, RC). The curves overplotted on the distributions represent models of the uncertainty distributions assuming Gaussian statistics. Under the assumption that all stars in K2 have the same, true fractional uncertainty, σ , these distributions would be described by generalized gamma distributions with probability density function $f(x, a, d, p) = \frac{(p/a^d)x^{d-1}e^{-(x/a)^p}}{\Gamma(d/p)}$, where $\Gamma(z)$ denotes the gamma function, $p = 2$, $d = \text{dof} - 1$, and $a = \sqrt{2\sigma^2/(\text{dof} - 1)}$, where dof (degrees of freedom) corresponds to the number of pipelines contributing results for a star. We consider two models: one with σ fixed to be the observed median fractional uncertainty for each dof, and one with two generalized gamma distributions for which both σ and dof are allowed to vary. The gray (black) curves in Figures 20–21 are weighted sums of the best-fitting single-component (two-component) models across all dof (see the Appendix for details). It is clear that the observed distributions of $\sigma_{\nu'_{\max}}/\langle\nu'_{\max}\rangle$ and $\sigma_{\Delta\nu'}/\langle\Delta\nu'\rangle$ are not perfectly described by a

generalized gamma distribution with a unique σ , as they would be if all stars had the same fractional uncertainty in $\langle\nu'_{\max}\rangle$ and $\langle\Delta\nu'\rangle$. Nevertheless, allowing σ to be a function of the number of reporting pipelines, dof, appears to be a surprisingly good approximation. This indicates that (1) the fractional uncertainties for all stars are not a strong function of ν_{\max} or $\Delta\nu$ (but rather have a fractional uncertainty that varies modestly according to the number of reporting pipelines) and (2) our uncertainty estimates are distributed like they should be according to χ statistics. As we note in the Appendix, the fractional uncertainties vary mostly according to the evolutionary state, with RC parameters being less precisely measured, and it happens that the typical uncertainties are the same for ν_{\max} and $\Delta\nu$ for RGB stars. Our typical uncertainties for $\langle\nu'_{\max}\rangle$ and $\langle\Delta\nu'\rangle$ are listed in Table 7, along with the corresponding median fractional uncertainties from APOKASC-2 (Pinsonneault et al. 2018) (“APOKASC-2” in the table). We also include a comparison to the median fractional uncertainties from the analysis of Yu et al. (2018) (“Y18” in the table). The latter analysis uses only the SYD pipeline, as opposed to APOKASC-2, which reports parameters averaged across five different asteroseismic pipelines. The methodology in this work is much the same as that of Pinsonneault et al. (2018), but we include a comparison to Yu et al. (2018) to give an indication of the variation in uncertainties resulting from an aggregated pipeline versus individual pipeline approach. The most significant difference between the uncertainties of the two Kepler analyses is in RC ν_{\max} , for which uncertainties from Yu et al. (2018) are larger than those from APOKASC-2; the larger ν_{\max} uncertainties from Yu et al. (2018) map into correspondingly larger RC κ'_R and κ'_M uncertainties. Comparing our results to those of APOKASC-2, we see that the uncertainties in ν_{\max} in K2 are up to a factor of two larger than in Kepler, and the uncertainties in $\Delta\nu$ are larger by up to a factor of four for RGB stars. These differences between Kepler and K2 come from differences in photometric precision and the differences in dwell time, and will be further explored in the next K2 GAP data release.

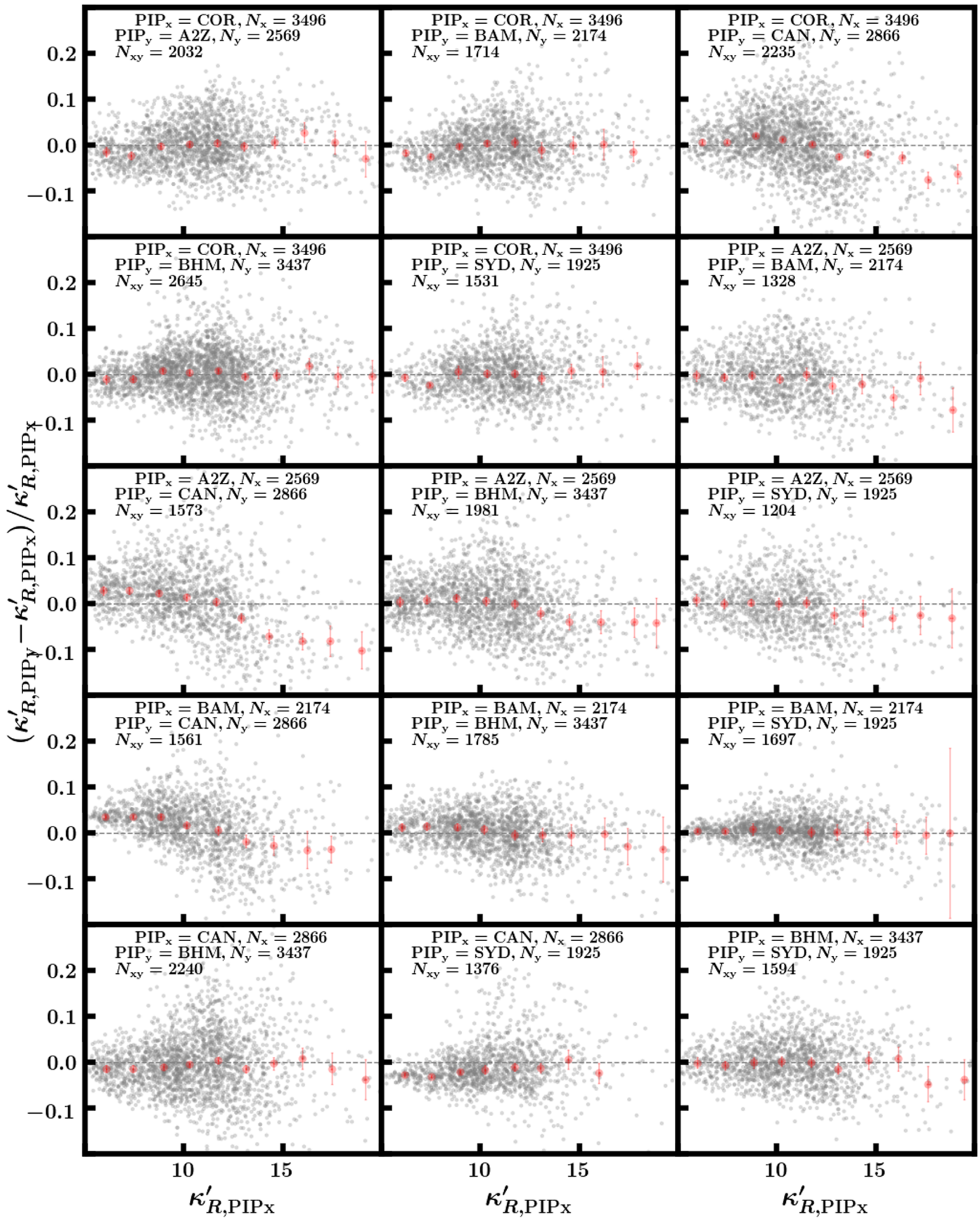


Figure 10. Pairwise comparisons between asteroseismology pipeline κ'_R values for K2 GAP DR3. Red error bars represent binned medians and uncertainties on those binned medians. N_x and N_y indicate the number of stars with nonzero asteroseismic values and uncertainties returned for pipeline x and pipeline y , with the number of stars returned by both pipelines indicated by N_{xy} .

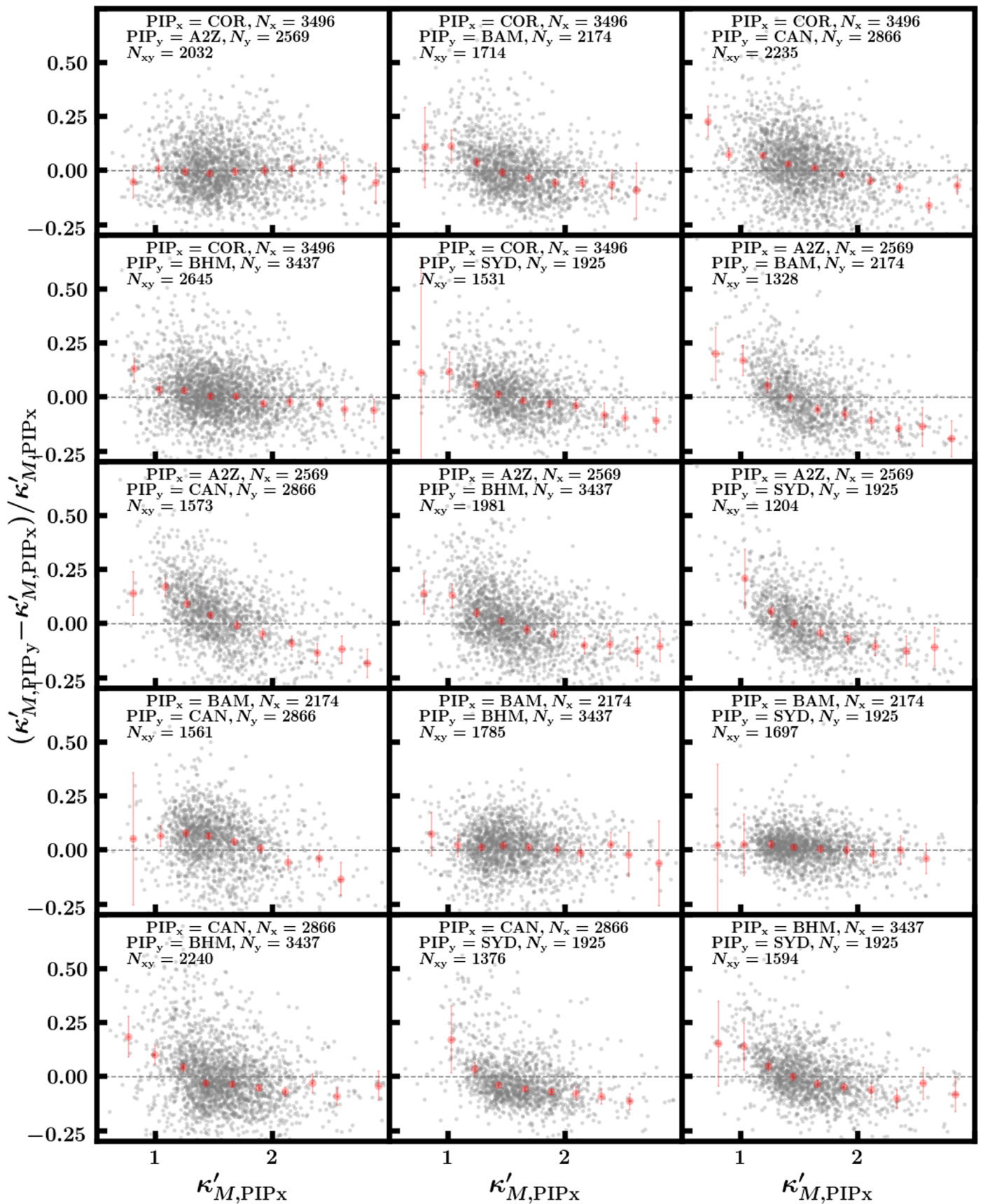


Figure 11. Same as in Figure 10, but for κ'_M .

Table 6
Radius and Mass Coefficients

EPIC	$\langle \kappa'_R \rangle$	$\sigma_{\langle \kappa'_R \rangle}$	$\langle \kappa'_M \rangle$	$\sigma_{\langle \kappa'_M \rangle}$	$\kappa'_{R,A2Z}$	$\sigma_{\kappa'_{R,A2Z}}$	$\kappa'_{M,A2Z}$	$\sigma_{\kappa'_{M,A2Z}}$	$\kappa'_{R,BAM}$	$\sigma_{\kappa'_{R,BAM}}$	$\kappa'_{M,BAM}$	$\sigma_{\kappa'_{M,BAM}}$	$\kappa'_{R,BHM}$	
210306475	12.976	0.906	1.559	0.265	12.209	0.964	1.381	0.327	12.556	
210307958	10.987	0.767	1.137	0.179	9.900	...	0.889	...	12.072	0.834	1.430	0.212	...	
210314854	10.555	0.446	1.119	0.124	9.909	0.898	0.925	0.222	10.668	0.492	1.174	0.124	10.668	
210315825	9.521	0.160	1.751	0.066	9.582	0.773	1.776	0.375	9.517	0.291	1.737	0.139	9.354	
210318976	11.953	0.677	1.137	0.136	12.862	1.022	1.331	0.309	
$\sigma_{\kappa'_{R,BHM}}$	$\kappa'_{M,BHM}$	$\sigma_{\kappa'_{M,BHM}}$	$\kappa'_{R,CAN}$	$\sigma_{\kappa'_{R,CAN}}$	$\kappa'_{M,CAN}$	$\sigma_{\kappa'_{M,CAN}}$	$\kappa'_{R,COR}$	$\sigma_{\kappa'_{R,COR}}$	$\kappa'_{M,COR}$	$\sigma_{\kappa'_{M,COR}}$	$\kappa'_{R,SYD}$	$\sigma_{\kappa'_{R,SYD}}$	$\kappa'_{M,SYD}$	$\sigma_{\kappa'_{M,SYD}}$
1.304	1.372	0.327	13.793	1.360	1.807	0.367
...	10.390	0.598	1.037	0.145	10.883	0.560	1.088	0.133	11.509	1.234	1.248	0.274
1.033	1.148	0.237	10.823	0.603	1.177	0.183	10.277	0.478	1.083	0.122	10.961	1.309	1.221	0.302
0.612	1.698	0.237	9.644	0.337	1.814	0.154	9.299	0.331	1.652	0.141	9.740	0.275	1.839	0.134
...	11.166	0.804	0.969	0.179	11.797	0.620	1.106	0.138

Notes. Here, $\langle \kappa'_R \rangle$ and $\langle \kappa'_M \rangle$, as well as their uncertainties, are computed based on $\langle \Delta \nu' \rangle$ and $\langle \nu'_{\max} \rangle$, according to Equations (4) and (6), and represent pipeline-averaged radius and mass coefficients. Pipeline-specific radius and mass coefficients, $\kappa'_{R,i}$ and $\kappa'_{M,i}$, are computed with pipeline-specific asteroseismic parameters, $\Delta \nu'_i$ and $\nu'_{\max,i}$. See Section 3.2.4 for details.

(This table is available in its entirety in machine-readable form.)

Table 7
Median Fractional Uncertainties of Kepler and K2 Asteroseismic Quantities (in Percent)

	RGB/		RC			
	RGB or	AGB	RC	RC		
	APOKASC-2	Y18	K2	APOKASC-2	Y18	K2
$\sigma_{\nu_{\max}}$	0.9	1.0	1.7	1.3	2.1	2.4
$\sigma_{\Delta\nu}$	0.4	0.3	1.7	1.1	1.1	2.3
σ_{κ_R}	1.3	1.1	3.3	2.7	3.3	5.0
σ_{κ_M}	3.4	3.1	7.7	6.2	8.4	10.5

Notes. “APOKASC-2” indicates median fractional uncertainties from the analysis of Pinsonneault et al. (2018), while “Y18” refers to the analysis of Yu et al. (2018).

The analogous uncertainty distributions for $\langle\kappa'_R\rangle$ and $\langle\kappa'_M\rangle$ are shown in Figures 22–23. Note that the number of stars plotted, N , is not 4395 (the total number of stars we provide with $\langle\kappa'_R\rangle$ and $\langle\kappa'_M\rangle$). This is because, in this treatment, we require the number of pipelines reporting values for ν_{\max} and $\Delta\nu$ be the same in order to fulfill the generalized gamma distribution requirements; most stars do not have the same number of ν_{\max} measurements as $\Delta\nu$: there are 1030 such RGB stars and 257 such RC stars. Considering the excellent match of the fitted generalized gamma distributions (black), we adopt the fitted σ as statistical uncertainties for $\langle\kappa'_R\rangle$ and $\langle\kappa'_M\rangle$ as listed in Table 7. We also list the corresponding median fractional uncertainties in Kepler, computed using the evolutionary states and ν_{\max} and $\Delta\nu$ values from Pinsonneault et al. (2018) (“APOKASC-2”) or those from Yu et al. (2018) (“Y18”). We find that the K2 radius (mass) uncertainties are larger by up to a factor of three (two) compared to that of Kepler for RGB stars from APOKASC-2. The uncertainties in RC stellar parameters are more comparable between the two data sets, with the increase in uncertainty from Kepler to K2 not being larger than a factor of two. The uncertainties are more comparable between Yu et al. (2018) results and K2 because of the larger uncertainty in RC ν_{\max} from Yu et al. (2018) compared to APOKASC-2.

3.4. Systematic Uncertainties in $\langle\nu'_{\max}\rangle$, $\langle\Delta\nu'\rangle$, $\langle\kappa'_R\rangle$, and $\langle\kappa'_M\rangle$

We now turn to systematic uncertainties in $\langle\nu'_{\max}\rangle$, $\langle\Delta\nu'\rangle$, $\langle\kappa'_R\rangle$, and $\langle\kappa'_M\rangle$ that take the form of ν_{\max} - and $\Delta\nu$ -dependent offsets among the pipelines. By definition, the rescaling process described in Section 3.2.1 removes offsets among the pipelines by averaging over all ν_{\max} and $\Delta\nu$. However, there are ν_{\max} - and $\Delta\nu$ -dependent trends seen in the fractional differences in $\langle\nu'_{\max}\rangle$ and $\langle\Delta\nu'\rangle$ shown in Figures 6–9. Our approach to account for these systematics is to adopt the largest excursion of any pipeline from $\langle\nu'_{\max}\rangle$ and $\langle\Delta\nu'\rangle$ for each bin plotted in the bottom panel of Figures 6–9, add to that the uncertainty on the median, and adopt the result as 2σ systematic uncertainties. The resulting (1σ) uncertainties are listed in Table 8. For most stars, the typical systematic uncertainty is less than the statistical uncertainty: for a typical RGB star with $(\nu_{\max}, \Delta\nu) \sim (75, 7.5 \mu\text{Hz})$ or RC star with $(\nu_{\max}, \Delta\nu) \sim (30, 4.0 \mu\text{Hz})$, the systematic uncertainties are similar, at $\sim 0.6\%$ in $\langle\nu'_{\max}\rangle$ and $\sim 0.3\%$ in $\langle\Delta\nu'\rangle$. We adopt these numbers as typical systematic uncertainties for $\langle\nu'_{\max}\rangle$ and $\langle\Delta\nu'\rangle$, though they are clearly a function of ν_{\max} and $\Delta\nu$.

Generally, though, the uncertainty is larger at smaller ν_{\max} and $\Delta\nu$. This is a result both of having intrinsically fewer stars in this regime (as they are more evolved and therefore shorter-lived) as well as there being difficulties in measuring low-frequency ν_{\max} and $\Delta\nu$ due to the K2 frequency resolution. We take the systematic uncertainties in $\langle\kappa'_R\rangle$ and $\langle\kappa'_M\rangle$ to be 1% and 2%, from propagation of the systematic uncertainties in $\langle\nu'_{\max}\rangle$ and $\langle\Delta\nu'\rangle$. As with $\langle\nu'_{\max}\rangle$ and $\langle\Delta\nu'\rangle$, in detail, these systematic uncertainties are a function of $\langle\kappa'_R\rangle$ and $\langle\kappa'_M\rangle$ (see Figures 10 and 11).

We note that the $\Delta\nu$ correction applied to $\langle\Delta\nu'\rangle$ and therefore $\langle\kappa'_R\rangle$ and $\langle\kappa'_M\rangle$, X_{Sharma} , is computed using the EPIC temperature and metallicity scale. We acknowledge that the user may wish to use their own temperatures, and therefore we caution that using a different temperature scale will introduce systematics. For example, using a temperature scale 100 K hotter (cooler) than the EPIC temperature will make radii 1% lower (higher) if X_{Sharma} is not also recomputed with the user’s adopted temperatures. In order to give the user as much convenience as possible, we provide EPIC temperatures in Table 4, should the user wish to compute consistent radii/masses; we also include the EPIC metallicities used for computing X_{Sharma} . In the event the user wishes to use a different temperature scale and does not wish to sustain additional $\sim 1\%$ systematic uncertainties, we encourage recomputing X_{Sharma} with the user’s own temperatures and/or metallicities using `asfgrid` (Sharma & Stello 2016; Sharma et al. 2016), which is available at <http://www.physics.usyd.edu.au/k2gap/Asfgrid/>.

4. Results

4.1. Comparison to Galaxia

We start by comparing properties of the K2 GAP DR2 sample to those of a Galaxia simulation (Sharma et al. 2011), with corrections made to the simulated metallicity scale described in Sharma et al. (2019). Each campaign has been modeled separately because they each probe different regions of the Galaxy. To make the simulated populations comparable to the data, we select only the simulated stars that would be seismically detected. We defined the detectable sample to be stars with $3 \mu\text{Hz} < \nu_{\max} < 280 \mu\text{Hz}$ and signal-to-noise ratio yielding a probability of detection greater than 95% (calculated according to the procedure used in Chaplin et al. (2011)). We impose the same selection of the simulated and observed stars (see Section 2.1 and also Sharma et al. (2019)), using a synthetic V-band magnitude that depends on $J - K_s$ color according to $V = K_s + 2.0((J - K_s) + 0.14) + 0.382e^{2(J - K_s - 0.2)}$ (Sharma et al. 2018).

Galaxia models of the magnitude- ν_{\max} distributions show good agreement with the observations, as shown in Figures 12–14. The most obvious feature in these plots is the RC, which, because red giants spend a relatively long amount of time in this phase, results in a “clump” of stars at $\nu_{\max} \sim 30 \mu\text{Hz}$. Lower-gravity (lower- ν_{\max}) red giants oscillate with larger power than higher-gravity red giants, and so at a fixed magnitude, it is easier to measure oscillations in lower-gravity red giants. The amplitude of oscillations is primarily a function of surface gravity (Kallinger et al. 2014), and so the diagonal cutoff in the top right corner of both Galaxia predictions and (for the most part) observations is a result of the signal-to-noise ratio from the surface gravity-dependent oscillation amplitude compared to the magnitude-dependent white noise. To demonstrate this ν_{\max} -dependent white noise limit, we assume a detectability threshold of

Table 8
Systematic Uncertainties of $\langle \nu'_{\max} \rangle$ and $\langle \Delta \nu' \rangle$, as a Function of $\langle \nu'_{\max} \rangle$ and $\langle \Delta \nu' \rangle$

$\langle \nu'_{\max} \rangle_{\text{RGB}}$ (μHz)	$\sigma_{\langle \nu'_{\max} \rangle, \text{RGB}}$ (%)	$\langle \nu'_{\max} \rangle_{\text{RC}}$ (μHz)	$\sigma_{\langle \nu'_{\max} \rangle, \text{RC}}$ (%)	$\langle \Delta \nu' \rangle_{\text{RGB}}$ (μHz)	$\sigma_{\langle \Delta \nu' \rangle, \text{RGB}}$ (%)	$\langle \Delta \nu' \rangle_{\text{RC}}$ (μHz)	$\sigma_{\langle \Delta \nu' \rangle, \text{RC}}$ (%)
12	0.67	23	1.2	1.7	1.3	3.4	0.85
17	0.91	28	0.83	2.3	1.0	3.7	0.52
23	0.64	31	0.24	2.9	0.68	4.1	0.24
30	0.40	38	0.68	3.8	0.31	4.5	0.47
42	0.29	43	0.74	4.9	0.28	5.1	0.66
56	0.55	53	1.1	5.8	0.21	5.7	0.75
76	0.68	62	0.69	7.1	0.24	6.3	0.59
110	0.73	73	0.92	9.3	0.40	7.0	0.68
140	0.70	84	1.2	11	0.43	7.7	0.92
190	0.50	93	1.4	15	0.81	8.7	0.43

Notes. Systematic uncertainties of $\langle \nu'_{\max} \rangle$ and $\langle \Delta \nu' \rangle$, listed as percentages. The binned medians of the fractional difference between an individual pipeline’s asteroseismic values and the mean values, $\langle \nu'_{\max} \rangle$ and $\langle \Delta \nu' \rangle$, shown in the bottom panels of Figures 6–9 are taken to be indications of systematic uncertainty in $\langle \nu'_{\max} \rangle$ and $\langle \Delta \nu' \rangle$; see Section 3.4 for details.

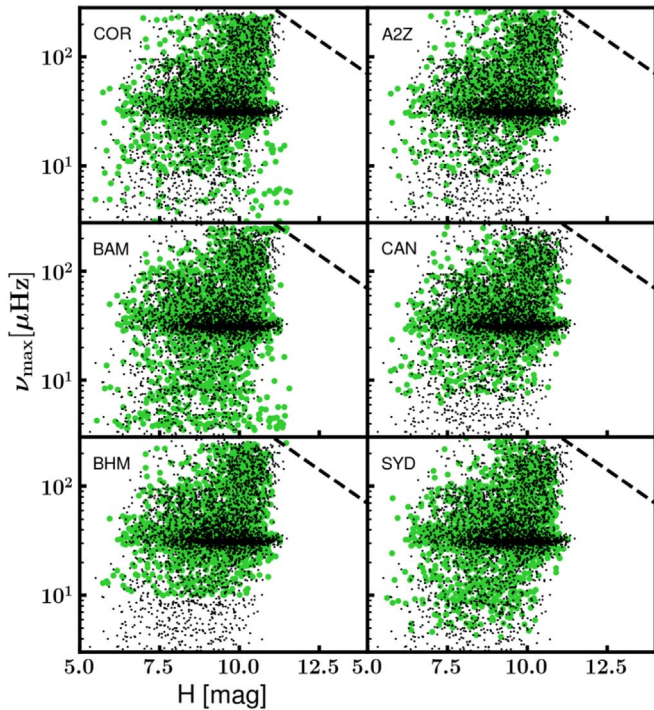


Figure 12. Distributions of ν_{\max} as a function of magnitude, as predicted by *Galaxia* (black) and observed (green) for K2 C4. Dashed lines represent our adopted detectability threshold of $\nu_{\max, \text{detect}} < 5 \times 10^4 1.6^{-H}$.

$\nu_{\max, \text{detect}} < 5 \times 10^4 1.6^{-H}$ in Figures 12–14 (dashed lines). This detectability threshold describes the observed data well, and scales like a flux-dependent white noise would. In Kp -band space, this threshold would mean a detectability limit of $Kp \approx 15$, fainter than which the white noise is too large to detect high- ν_{\max} oscillators. Compared to the detectability threshold of C1 described in Stello et al. (2017), the dependence on magnitude is less steep, and likely reflects the improved noise qualities following improved pointing control starting with C3. The reason the faint and bright limits do not form straight, vertical trends in Figures 12–14, which show the H band, is because we selected stars in the V band (see Section 2.1). For convenience, we also show the detection distributions as a function of only H -band magnitude in Figure 15.

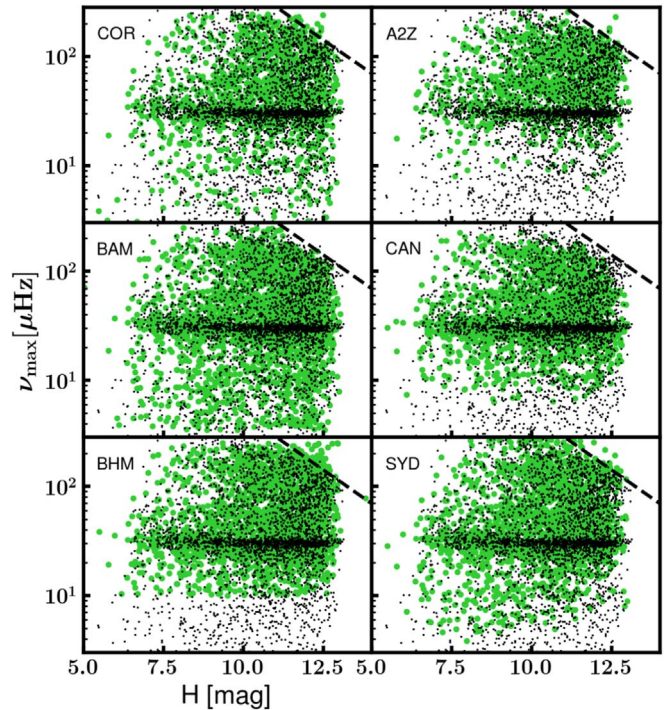


Figure 13. Same as Figure 12, but for K2 C6.

We condense the comparison between observed and simulated asteroseismic values to just the ν_{\max} dimension for C4 and C7 in Figures 16 and 17. The agreement is generally good. There are two main discrepancies, however. First, the number of predicted oscillators in C4 does not agree with the observations (Figure 16(a)). However, plotting the normalized distribution such that each bin is divided by the bin size (representing probability density) results in agreement, except for the low- ν_{\max} regime (Figure 16(b)). We discuss the discrepancy in Figure 16(a) below. Second, there are fewer observed low- ν_{\max} stars ($\nu_{\max} \lesssim 10\text{--}20 \mu\text{Hz}$) than predicted in both C4 and C7. Although Stello et al. (2017) found this same bias in K2 GAP DR1, we attempt to verify that it is not due to a bias in the *Galaxia* models themselves by manually inspecting all K2 GAP spectra in C6 for evidence of solar-

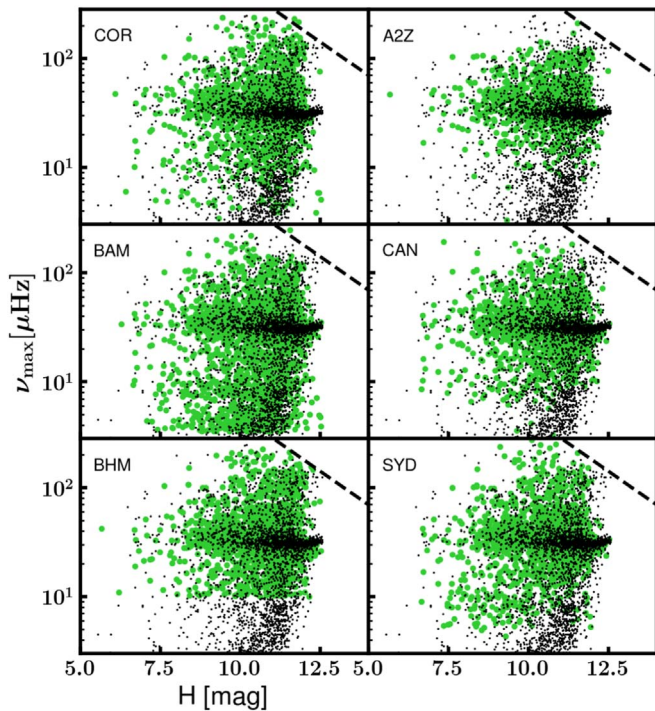


Figure 14. Same as Figure 12, but for K2 C7.

like oscillations. Two experts did the exercise separately, classifying the K2 spectra according to whether or not they had a detectable ν_{\max} (yes/maybe/no), additionally assigning a visual estimate of ν_{\max} . Objects that showed evidence of solar-like oscillations below the effective high-pass cutoff of $3 \mu\text{Hz}$ were classified as “no.” Note that this exercise did not require the detection of $\Delta\nu$ for classification as a solar-like oscillator, which is consistent with our definition of a pipeline detection as a valid ν_{\max} measurement (see Section 3.1). The results from each person were nearly identical, with any contested classifications discussed individually and a final consensus classification agreed upon.

As evident in Figure 18, the predicted ν_{\max} distribution from *Galaxia* is in good agreement with the visually confirmed distribution (classifications of “yes” are plotted, but those of “maybe” are not), though they are formally inconsistent with being drawn from the same distribution, according to a Kolmogorov–Smirnov test. By going through all of the observed targets by eye and not just ones that were returned by pipelines as being red giants, we are able to be more confident that the *Galaxia* predictions are robust and not subject to obvious biases. The distributions of ν_{\max} returned by individual pipelines all fall short of being formally consistent with either the visually confirmed distribution or the *Galaxia* distribution, though some of the pipeline ν_{\max} distributions qualitatively show good agreement with the predicted and visually confirmed distributions.

As noted above, there is nonetheless a bias against detecting stars with ν_{\max} below $\sim 10\text{--}20 \mu\text{Hz}$. This is true for all three of the campaigns, which indicates that this detection bias was not solely a function of the particular DR1 sample, which were all in C1. With the data we have in hand, we cannot definitively say what causes this bias. At these low frequencies, there are relatively few modes observable. This may hinder detecting these oscillations for any pipeline that relies on finding $\Delta\nu$ as part of its ν_{\max} detection step, and can also hamper fits to the

power excess using a Gaussian, since a Gaussian does not perform well at describing a few discrete modes. It is also possible that low- ν_{\max} oscillators are harder to recover at lower frequencies because of the relatively short K2 dwell time, which leads to a smaller ratio of the frequency resolution to the mode width; the result is that the spectra of these stars can sometimes be hard to distinguish from a pure granulation background. The degree to which these oscillators are detected or not is highly pipeline-dependent, as one can see from Figures 16–18.

Keeping this low- ν_{\max} detection bias in mind, we can go on to test the detection rate for $\nu_{\max} > 20 \mu\text{Hz}$, using *Galaxia* and visual inspection as ground truths. In C7, there are 1740 such stars that have asteroseismic values from at least one pipeline. This number is consistent with the 1758 expected stars from the *Galaxia* simulation for C7. The number of stars (2312) recovered by at least one pipeline in C6 is between the number found by visual inspection (2214) and that predicted by *Galaxia* (2511). In C4, however, there are significantly fewer stars observed by at least one pipeline than predicted by *Galaxia* (2177 versus 2670). These “missing” stars are at magnitudes $K_p < 13$, and therefore should yield observable asteroseismic parameters, given our empirical detectability threshold. The *Galaxia* model seems to under-predict reddening in this campaign, which may explain this discrepancy. Indeed, the predicted fraction of dwarfs (and therefore the fraction of stars that would not be detected as oscillators in long-cadence K2 data) depends on the assumed reddening. For K2 GAP, the selection “draws a line” in $J - K_s$ color space to separate the sample of predominantly blue dwarfs from the sample containing the red giants (and some red dwarfs), which are the targets with $J - K_s > 0.5$. The same cut is applied to the synthetic stellar population in the *Galaxia* simulation, using an assumed reddening. An underestimated reddening in *Galaxia* means that fewer of the blue dwarfs are reddened enough to fall on the giant side of the $J - K_s > 0.5$ dwarf/giant dividing line, increasing the number of predicted oscillators compared to reality.

4.2. Absolute Radius Calibration

The derived $\langle \Delta\nu' \rangle$ and $\langle \nu'_{\max} \rangle$ have not necessarily been placed on an absolute scale. While we scaled the asteroseismic values to a common mean scale, we were free to impose solar reference values for $\langle \nu'_{\max} \rangle$ and $\langle \Delta\nu' \rangle$ to be $\nu_{\max,\odot} = 3076 \mu\text{Hz}$ and $\Delta\nu_{\odot} = 135.146 \mu\text{Hz}$, which are relatively close to the average pipeline-specific solar reference values, and which are the same as determined by the absolute asteroseismology rescaling done in the APOKASC-2 analysis. Were we working with Kepler data and using the same pipelines as in the APOKASC-2 analysis, this choice of solar reference values would be valid and would put the asteroseismic radii on a scale that is consistent with open cluster masses and Gaia radii (Pinsonneault et al. 2018; Zinn et al. 2019b). There are at least two reasons why choosing our solar reference values as $\nu_{\max,\odot} = 3076 \mu\text{Hz}$ and $\Delta\nu_{\odot} = 135.146 \mu\text{Hz}$ may not result in $\langle \kappa'_R \rangle$ and $\langle \kappa'_M \rangle$ being on an absolute scale. First, although our rescaling procedure to derive $\langle \Delta\nu' \rangle$ and $\langle \nu'_{\max} \rangle$ is nearly the same as in Pinsonneault et al. (2018), we have added BAM as one of the pipelines that contributes to the rescaling procedure: APOKASC-2 used results from A2Z, CAN, COR, SYD, and OCT, and in this work, we have used results from A2Z, CAN, COR, SYD, BHM (based on OCT), and BAM (see Section 3.1

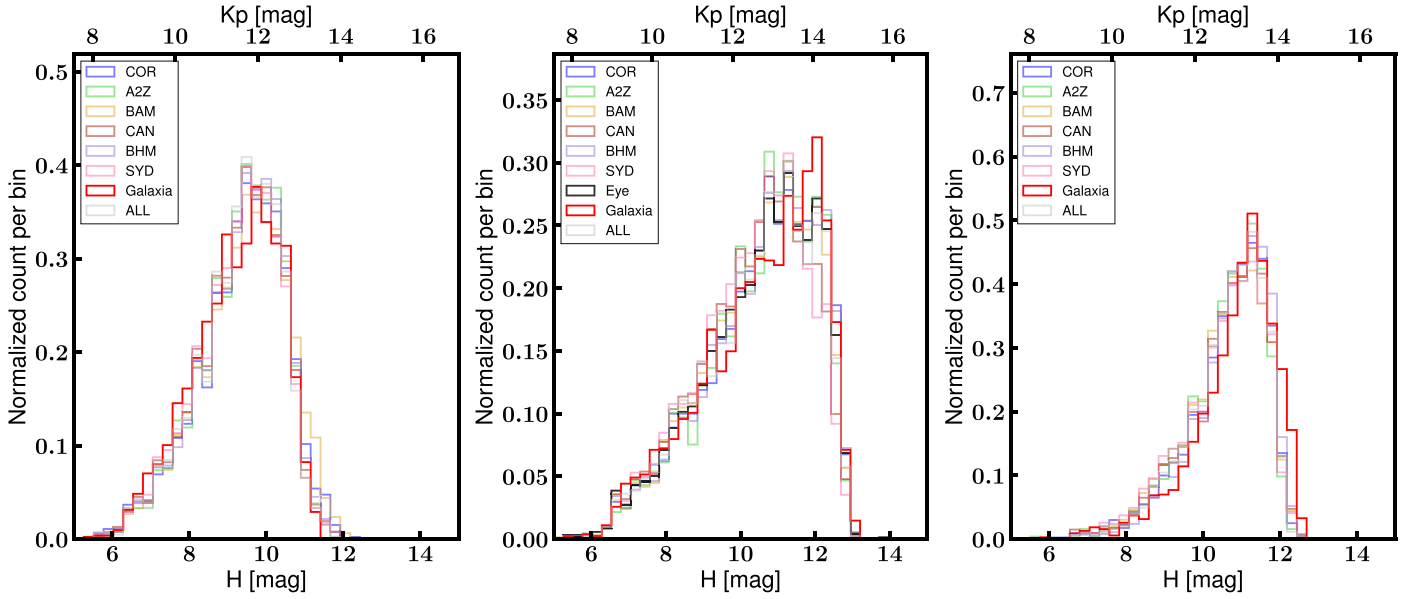


Figure 15. Distributions of H -band magnitude for C4 (left), C6 (middle), and C7 (right), as predicted by *Galaxia* (red) and observed for each pipeline, according to the legend. Distribution of stars with $\langle \nu'_{\max} \rangle$ is labeled as “ALL”—this is not the same as summing the individual pipeline histograms, because not every star will have a $\langle \nu'_{\max} \rangle$, as that requires at least two pipelines reporting values. Approximate Kp -band scale is indicated on the top x -axis.

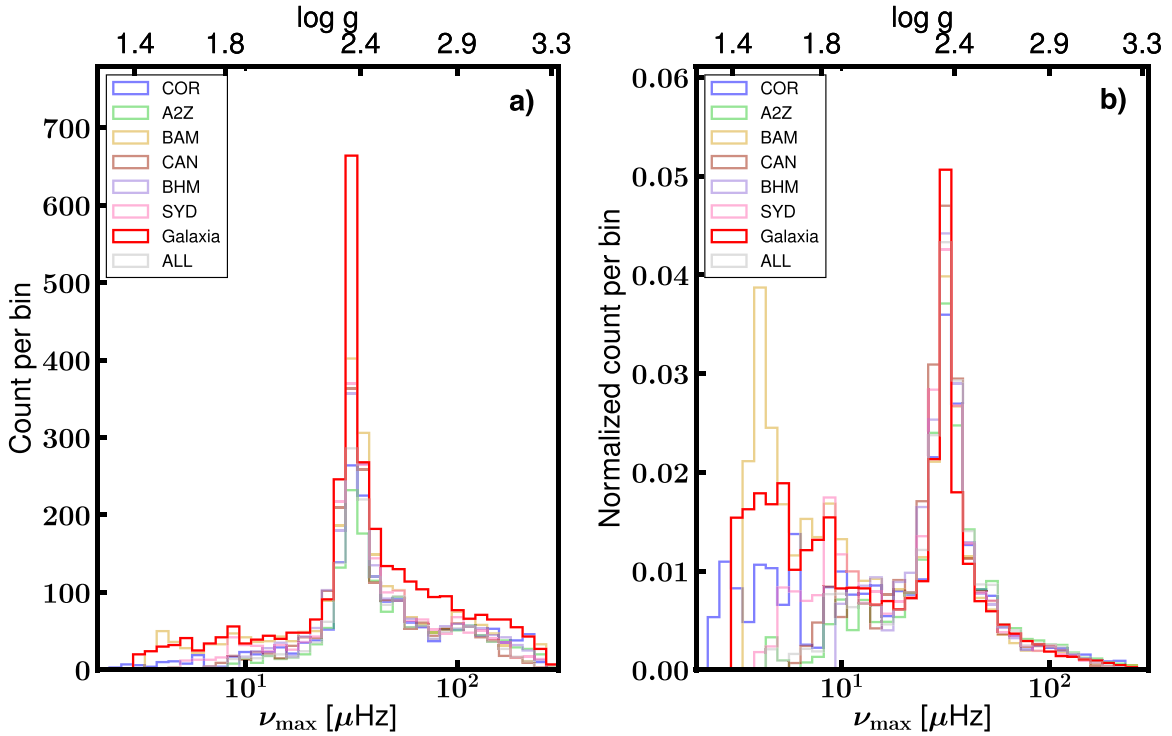


Figure 16. Left: distributions of ν_{\max} for stars that have been recovered by a particular pipeline (i.e., observed; colored according to the legend) compared to the *Galaxia* simulation of predicted detections for K2 C4 (red). Approximate asteroseismic surface gravity scale was computed with scaling relations according to Equation (1), and assuming a temperature of 4500 K. Right: same as left, but showing normalized counts such that the distributions represent probability density.

for summaries of the pipeline methodologies). The addition of BAM in this work to the pipelines used for aggregating asteroseismic results may result in a slightly different mean scale for $\langle \nu'_{\max} \rangle$ and $\langle \Delta \nu' \rangle$. This is because the APOAKSC-2 solar reference values were chosen such that the aggregated stellar masses agreed with open cluster masses—using a different set of pipelines to average over may have required a different set of solar reference values to achieve agreement with

open cluster masses. We see this in the differences between the rescaling values from our analysis and from that of Pinsonneault et al. (2018), shown in Table 5. Second, there is evidence to suggest that there are systematic biases in asteroseismic parameters based on the dwell time of the data (J. C. Zinn et al. 2020, in preparation), which could be suggestive of a need to modify the $\nu_{\max, \odot}$ and/or $\Delta \nu_{\odot}$ for K2 data compared to Kepler data. We now test this choice of zero

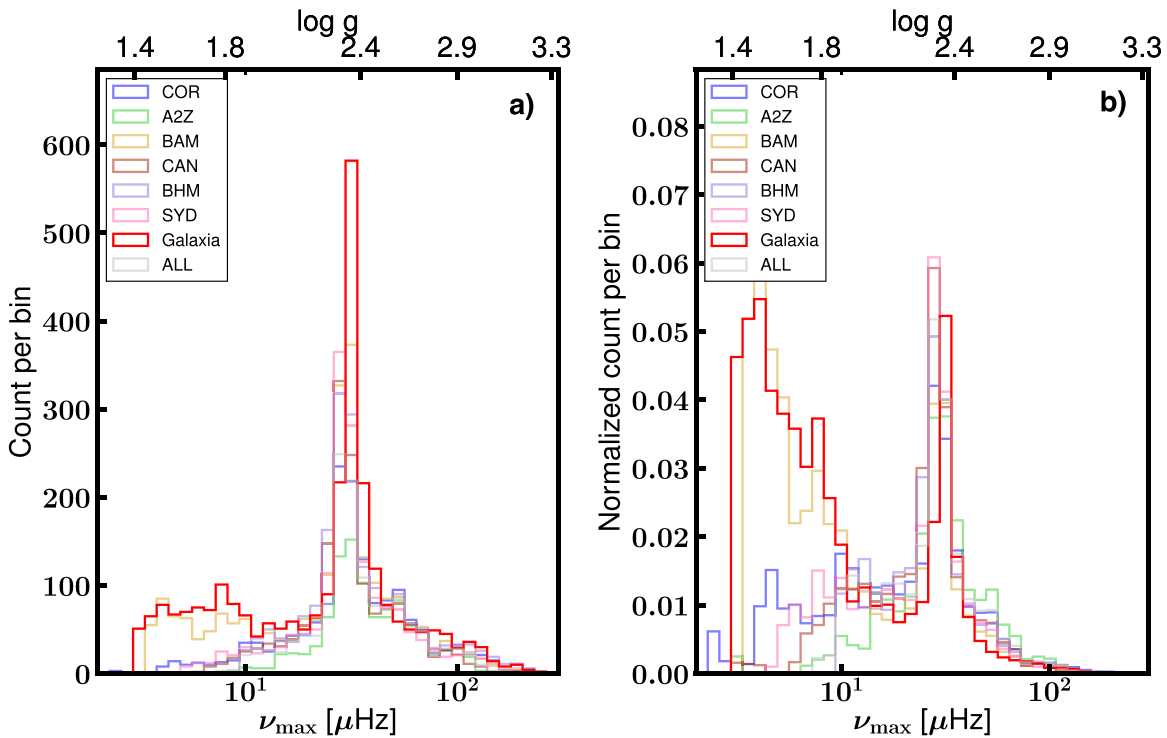


Figure 17. Same as Figure 16, but for C7.

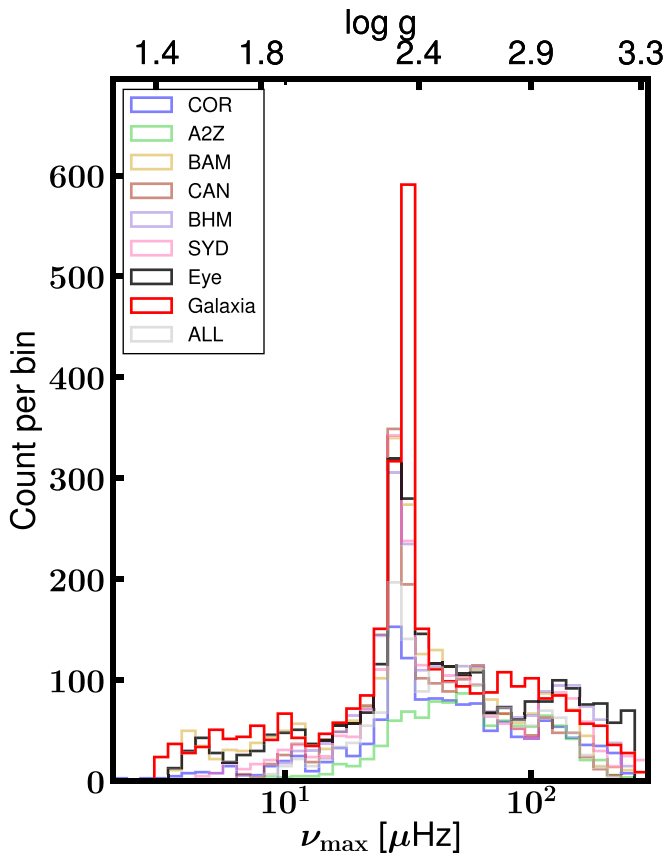


Figure 18. Distributions of ν_{\max} for stars that have been recovered by a particular pipeline (i.e., observed; colored according to the legend); that have a visible ν_{\max} as determined by eye (black); and that are expected to have a detectable ν_{\max} according to the *Galaxia* simulation (red) for K2 C6. Approximate asteroseismic surface gravity scale was computed with scaling relations according to Equation (1), and assuming a temperature of 4500 K.

points by comparing the derived radii to radii using parallaxes from Gaia Data Release 2 (Gaia Collaboration et al. 2018; Lindegren et al. 2018).

We populated the overlap sample of stars in K2 GAP DR2 with both $\langle \Delta\nu' \rangle$ and $\langle \nu'_{\max} \rangle$ and Gaia DR2 by matching on 2MASS ID using the Gaia Archive.²⁴ We also required APOGEE metallicities and temperatures from DR16 (Ahumada et al. 2020). Because of a known, position-, magnitude-, and color-dependent zero point in the Gaia parallaxes (e.g., Lindegren et al. 2018; Zinn et al. 2019a), we did not work directly with the Gaia DR2 parallaxes. Instead, we followed the methodology of Schönrich et al. (2019) to derive distance estimates for stars in our K2 GAP sample. We did this separately for RC and RGB stars, with the understanding that RGB and RC populations will have different selection functions, which is an important consideration in the Bayesian distance estimates in the Schönrich et al. (2019) framework (see also Schönrich & Aumer 2017).

For the purposes of establishing a Gaia calibration of $\nu_{\max, \odot}$ and $\Delta\nu_{\odot}$, we used only stars with more than two pipelines returning results for $\Delta\nu$, and only considered stars with $\pi > 0.4$ and Gaia *G*-band < 13 mag in order to ensure that the results are less sensitive to any residual Gaia parallax zero points that may not be accounted for in the Schönrich et al. (2019) method; $[\text{Fe}/\text{H}] > -1$ to ensure that there are no metallicity-dependent asteroseismic radius systematics (see Zinn et al. 2019b); and $R < 30R_{\odot}$ to ensure there are no radius-dependent asteroseismic radius systematics (see Zinn et al. 2019b). For this sample, which has spectroscopic information, we recomputed $\Delta\nu$ correction factors using metallicities that are adjusted to account for nonsolar alpha abundances according to the Salaris et al. (1993)

²⁴ <https://gea.esac.esa.int/archive/>

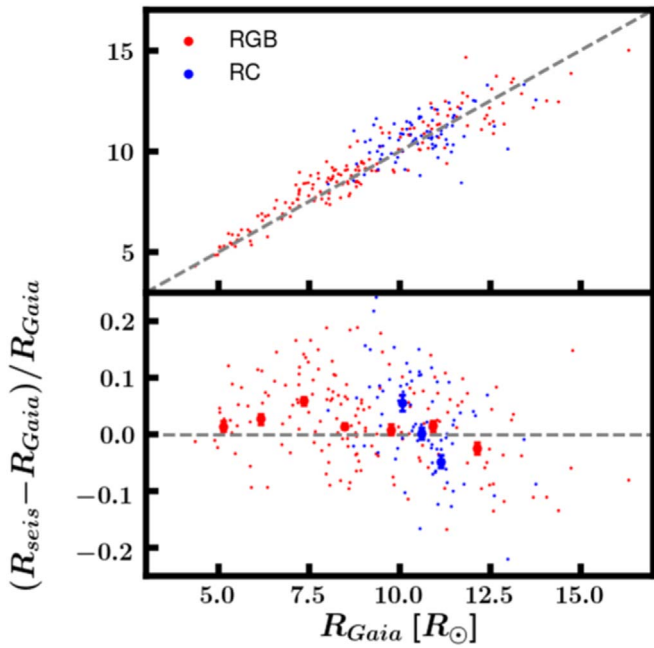


Figure 19. Comparison of asteroseismic scaling relation radii (Equation (4)) using K2 GAP DR2 $\langle \kappa'_R \rangle$ in combination with APOGEE effective temperatures and Gaia DR2 radii derived based on corrected Gaia parallaxes (see text). Gray dashed lines show one-to-one relations. In the bottom panel, error bars indicate weighted averages and standard errors on the weighted averages for RC stars (blue) and RGB stars (red).

prescription: $[\text{Fe}/\text{H}]' = [\text{Fe}/\text{H}] + \log_{10}(0.638 \times 10^{(\alpha/M)} + 0.362)$. We computed a Gaia radius for the 261 resulting stars, following a Monte Carlo procedure of the sort detailed in Zinn et al. (2017). The method uses the Stefan-Boltzmann law to translate the flux, temperature, and distance of a star into a radius. To do so, we computed bolometric fluxes with a K_s -band bolometric correction (González Hernández & Bonifacio 2009), APOGEE effective temperatures, and metallicities, combined with asteroseismic surface gravities from $\langle \nu'_{\text{max}} \rangle$. Extinctions were computed using the three-dimensional dust map of Green et al. (2015), as implemented in `mw dust`²⁵ (Bovy et al. 2016). Five stars with asteroseismic and Gaia radii discrepant at more than the 3σ level were removed from subsequent analysis.

We compare the Gaia radius scale to our K2 asteroseismic radius scale in Figure 19. The top panel shows the points colored by evolutionary state (RGB in red and RC in blue), and the bottom panel shows the fractional agreement of the two radius scales. Figure 19 indicates that the radius scale of $\langle \kappa'_R \rangle$ is consistent with the Gaia radius scale for both RC and RGB stars to within $\sim 3\%$. We find that the RGB stars are in more disagreement than the RC stars: while the median agreement is $3.0\% \pm 0.4\%$ for RGB stars, it is $1.6\% \pm 0.8\%$ for RC stars. This median statistic is computed as the median radius ratio for all RGB or RC stars, with the uncertainty in the median taken to be

$$\sigma_{\text{med}} = \sqrt{\frac{\pi}{2} \sum \sigma_R^2 / N^2}, \quad \text{where} \quad \sigma_R = \frac{R_{\text{seis}}}{R_{\text{Gaia}}} \sqrt{\left(\frac{\sigma_{R,\text{Gaia}}}{R_{\text{Gaia}}}\right)^2 + \left(\frac{\sigma_{R,\text{seis}}}{R_{\text{seis}}}\right)^2}.$$

Using the EPIC extinctions instead of those from Green et al. (2015) leads to insignificant variations in the radius agreement. However, the agreement is discrepant at the $\sim 3\sigma$ level between stars in C4 versus those in C7. This could be an indication of Gaia parallax zero-point issues, given that we do not expect such

variations in the asteroseismic data by campaign. We therefore also consider the Gaia zero point from Khan et al. (2019), who compared asteroseismic distances to Gaia distances in K2 C3 and C6. For this exercise, we restricted our sample to the stars in C6, and adopted their derived zero point of $-17 \mu\text{as}$. The result is that the asteroseismic radii are consistent with Gaia radii to within $\approx 1\%$ (RGB) and $\approx 5\%$ (RC).

Because the median agreement between the radius scales could be biased by underlying skewed distributions of the individual radii, we finally evaluate the agreement using a weighted mean: $\langle R_{\text{seis}}/R_{\text{Gaia}} \rangle = \frac{\sum R_{\text{seis}}/\sigma_R^2}{\sum 1/\sigma_R^2}$, where $\sigma_R = \frac{R_{\text{seis}}}{R_{\text{Gaia}}} \sqrt{\left(\frac{\sigma_{R,\text{Gaia}}}{R_{\text{Gaia}}}\right)^2 + \left(\frac{\sigma_{R,\text{seis}}}{R_{\text{seis}}}\right)^2}$. We calculate this for those stars that have fractional parallax uncertainties less than 10%, in order to mitigate potential biases due to parallax systematics. According to this metric, the agreement becomes $2.2\% \pm 0.3\%$ for RGB stars and $2.0\% \pm 0.6\%$ for RC stars.

Due to the variation in this agreement based on the tests described above, we opt not to rescale our $\langle \nu'_{\text{max}} \rangle$ or $\langle \Delta \nu' \rangle$ values, and instead allow for a systematic zero-point uncertainty in our derived $\langle \kappa'_R \rangle$ values. Acknowledging these uncertainties in the K2–Gaia agreement, we take the weighted mean estimate of the radius scales using the Schönrich et al. (2019) Gaia distances. Our asteroseismic radius coefficients could therefore be overestimated by up to $2.2\% \pm 0.3\%$ for RGB stars and up to $2.0\% \pm 0.6\%$ for RC stars. The uncertainty on this agreement is solely due to the standard uncertainty on the mean, and does not account for intrinsic scatter or trends in the radius agreement. Indeed, this should be thought of as being in addition to the systematic uncertainty from pipeline-to-pipeline variation in $\langle \kappa'_R \rangle$ as a function of ν_{max} and $\langle \Delta \nu' \rangle$ discussed in Section 3.4. We also note that this agreement does not account for systematic variation in the radius ratio due to choice of temperature, bolometric correction, or Gaia zero point, which may contribute to a systematic uncertainty of about $\pm 2\%$ (Zinn et al. 2019b).

Broadly speaking, the excellent level of agreement between asteroseismology and Gaia corroborates findings of the accuracy of the scaling relations in this regime from previous work based on asteroseismology–Gaia comparisons (Huber et al. 2017; Zinn et al. 2019b). In detail, there do appear to be trends with radius evident in Figure 19: the RGB radii appear to inflate compared to Gaia radii at around $R \sim 7.5 R_{\odot}$ (red error bars), while the red clump radii (blue error bars) seem to deflate compared to the Gaia radii with increasing radius at all radii. At least for the RC stars, systematics in the tracks used to generate the $\Delta \nu$ corrections could be to blame, particularly given the disagreement among RC models from the literature (An et al. 2019). Indeed, it appears that the RC radius trend is mostly a trend in $\Delta \nu$, with some metallicity dependence as well. At the population level, the RC radii have been found to agree within 5% with Gaia radii (Hall et al. 2019). However, to our knowledge, the scaling relations for RC stars have not been tested as a function of radius as we do here. We note also that a $\approx 1\%$ relative difference between the zero point for RGB versus RC stars is not ruled out by Pinsonneault et al. (2018) (see also Khan et al. 2019).

Regarding the mean agreement of RGB and RC stars, the most likely culprit for the (small) radius disagreement is a systematic in the solar reference value combination $\nu_{\text{max},\odot}/\Delta \nu_{\odot}^2$. That the absolute K2 asteroseismic radius scale is consistent with the Gaia radius scale to within $\sim 2\%$ naively

²⁵ <https://github.com/jobovy/mwdust>

implies that our $\langle \kappa'_M \rangle$ are within $\sim 6\%$ of an absolute mass scale, according to standard propagation of error from Equations (4) and (6). However, this is only approximate, because we can test only $\nu_{\max, \odot} / \Delta\nu_{\odot}^2$ against Gaia, whereas the mass coefficient goes as $\nu_{\max, \odot}^3 / \Delta\nu_{\odot}^4$.

In summary, because we are delivering asteroseismic values $\langle \nu'_{\max} \rangle$ and $\langle \Delta\nu' \rangle$ that are averaged values from several pipelines, we needed to evaluate to what extent the resulting asteroseismic scale is on an absolute scale. We did this by comparing to Gaia radii, and we found a systematic offset between the K2 GAP DR2 asteroseismic and Gaia radius scales of about 2%. This translates roughly to a 20% systematic uncertainty in age. Given the typical uncertainty in mass listed in Table 7, ages based on our RGB asteroseismic masses would be expected to have statistical uncertainties of $\approx 20\%$, with potential scale shifts by $\approx 20\%$ due to the level of systematics we identify in this section. This anticipated 20% statistical age uncertainty makes the data particularly interesting for potentially identifying the history of minor mergers in the Galaxy based on their impact on the age-velocity dispersion relation (Martig et al. 2014). For this and other Galactic archeology applications (e.g., age-abundance patterns), the 20% systematic uncertainty should not be significant, given that the differential age relationship between stellar populations would be preserved. Regarding mass- or magnitude-dependent systematics among RGB asteroseismic parameters, the small inflation of RGB asteroseismic radii at $R \sim 7.5R_{\odot}$ seems to map onto a corresponding trend in ν_{\max} , and so this may introduce an inflation in the RGB mass scale by perhaps up to 15% for the minority of stars with $50 \mu\text{Hz} \lesssim \langle \nu'_{\max} \rangle \lesssim 80 \mu\text{Hz}$. RC stars in our sample, on the other hand, appear to suffer from strong radius-dependent trends that seem to be related to the $\Delta\nu$ and not ν_{\max} scaling relation: there is a strong trend of RC agreement with $\Delta\nu$, which suggests that the $\Delta\nu$ scaling relation for RC stars is not well-calibrated using our $\Delta\nu$ corrections. Despite the concerning magnitude of the RC systematic, RC ages are not in popular use because of uncertainties in modeling mass loss (Casagrande et al. 2016). We will nonetheless explore the RC systematic further in the next and final K2 GAP data release, as having accurate red clump masses and radii is important for reckoning red clump models with observed red clump properties (e.g., An et al. 2019).

5. Conclusion

We have described the second data release of K2 GAP, containing red giants for campaigns 4, 6, and 7. We have derived evolutionary state classifications for our sample, and have placed the raw asteroseismic observations on a self-consistent scale, resulting in 4395 stars with mean asteroseismic parameters. We have also provided ready-to-use derived quantities, $\langle \kappa'_M \rangle$ and $\langle \kappa'_R \rangle$, for these stars, which yield masses and radii when combined with a weakly temperature-dependent factor that users may compute with their preferred effective temperature. We conclude the following:

1. The observed K2 GAP targets in campaigns 4, 6, and 7 have reproducible selection functions, which enable them for use in Galactic archeology studies.
2. ν_{\max} - and $\Delta\nu$ -dependent trends among pipelines have been improved by bringing the pipelines onto a common scale. This rescaling process effectively changes pipeline-specific solar reference values at or below the 1% level, in different measures, depending on the pipeline and the evolutionary state of the star.

3. We provide empirical uncertainties in ν_{\max} and $\Delta\nu$ values for stars that have results from at least two pipelines that have statistically reasonable distributions. These indicate that fractional uncertainties are not strong functions of ν_{\max} or $\Delta\nu$ or the number of pipelines reporting, but rather vary mostly according to evolutionary state: RGB stars have better-measured parameters than do RC stars. Systematic uncertainties for ν_{\max} and $\Delta\nu$ values are similar across evolutionary state, at $\sim 0.6\%$ and $\sim 0.3\%$ for both RGB and RC stars.
4. The distributions of our mean ν_{\max} are in good agreement with those predicted by theoretical stellar population synthesis models. Crucially, both the observed and predicted ν_{\max} distributions globally agree with an unbiased estimate of the ν_{\max} distributions from manual inspection of the data, which indicates our model predictions to be accurate, and our observed samples are largely complete. A notable exception to the asteroseismic detection completeness is for red giants with $\nu_{\max} \lesssim 10\text{--}20 \mu\text{Hz}$, where pipelines may report lower-than-expected numbers of oscillating stars.
5. The radius and mass coefficients that we provide, $\langle \kappa'_R \rangle$ and $\langle \kappa'_M \rangle$, have typical uncertainties of $\sigma_{\langle \kappa'_R \rangle} = 3.3\%$ (RGB or RGB/AGB) and $\sigma_{\langle \kappa'_R \rangle} = 5.0\%$ (RC) and $\sigma_{\langle \kappa'_M \rangle} = 7.7\%$ (RGB or RGB/AGB) and $\sigma_{\langle \kappa'_M \rangle} = 10.5\%$ (RC). These uncertainties are a factor of two to three higher than the uncertainties from Kepler radii and masses.
6. Our asteroseismic radii have been validated to be on the Gaia radius scale, to within $2.2\% \pm 0.3\%$ for RGB stars and $2.0\% \pm 0.6\%$ for RC stars.

K2 GAP Data Release 2 successfully builds upon K2 GAP DR1 in providing evolutionary state information, rescaled asteroseismic parameters and uncertainties that take advantage of the information from multiple asteroseismic pipelines, and radius and mass coefficients, in addition to placing the radius coefficients on an absolute scale. Future work will focus on calibrating the mass coefficients, which at this point cannot be definitively placed on an absolute scale, for lack of convenient mass calibrators in the sample. In the next K2 GAP data release, we may be able to place masses on an absolute scale, as we have done for radii in this work, by appealing to the red giant branch mass of open clusters observed by K2.

We thank the referee for comments that strengthened the manuscript. J. C. Z. and M. H. P. acknowledge support from NASA grants 80NSSC18K0391 and NNX17AJ40G. Y. E. and C. J. acknowledge the support of the UK Science and Technology Facilities Council (STFC). S. M. would like to acknowledge support from the Spanish Ministry with the Ramon y Cajal fellowship number RYC-2015-17697. R. A. G. acknowledges funding received from the PLATO CNES grant. R. S. acknowledges funding via a Royal Society University Research Fellowship. D.H. acknowledges support from the Alfred P. Sloan Foundation and the National Aeronautics and Space Administration (80NSSC19K0108). V.S.A. acknowledges support from the Independent Research Fund Denmark (Research grant 7027-00096B), and the Carlsberg foundation (grant agreement CF19-0649). This research was supported in part by the National Science Foundation under grant No. NSF PHY-1748958.

Funding for the Stellar Astrophysics Centre (SAC) is provided by The Danish National Research Foundation (grant agreement No. DNR106).

The K2 Galactic Archaeology Program is supported by the National Aeronautics and Space Administration under grant NNX16AJ17G issued through the K2 Guest Observer Program.

This publication makes use of data products from the Two Micron All Sky Survey, which is a joint project of the University of Massachusetts and the Infrared Processing and Analysis Center/California Institute of Technology, funded by the National Aeronautics and Space Administration and the National Science Foundation.

This work has made use of data from the European Space Agency (ESA) mission Gaia (<https://www.cosmos.esa.int/gaia>), processed by the Gaia Data Processing and Analysis Consortium (DPAC, <https://www.cosmos.esa.int/web/gaia/dpac/consortium>). Funding for the DPAC has been provided by national institutions, in particular the institutions participating in the Gaia Multilateral Agreement.

Funding for the Sloan Digital Sky Survey IV has been provided by the Alfred P. Sloan Foundation, the U.S. Department of Energy Office of Science, and the Participating Institutions. SDSS-IV acknowledges support and resources from the Center for High Performance Computing at the University of Utah. The SDSS website is www.sdss.org.

SDSS-IV is managed by the Astrophysical Research Consortium for the Participating Institutions of the SDSS Collaboration, including the Brazilian Participation Group, the Carnegie Institution for Science, Carnegie Mellon University, the Chilean Participation Group, the French Participation Group, the Harvard–Smithsonian Center for Astrophysics, Instituto de Astrofísica de Canarias, The Johns Hopkins University, Kavli Institute for the Physics and Mathematics of the Universe (IPMU)/University of Tokyo, the Korean Participation Group, Lawrence Berkeley National Laboratory, Leibniz Institut für Astrophysik Potsdam (AIP), Max-Planck-Institut für Astronomie (MPIA Heidelberg), Max-Planck-Institut für Astrophysik (MPA Garching), Max-Planck-Institut für Extraterrestrische Physik (MPE), National Astronomical Observatories of China, New Mexico State University, New York University, University of Notre Dame, Observatório Nacional/MCTI, The Ohio State University, Pennsylvania State University, Shanghai Astronomical Observatory, United Kingdom Participation Group, Universidad Nacional Autónoma de México, University of Arizona, University of Colorado Boulder, University of Oxford, University of Portsmouth, University of Utah, University of Virginia, University of Washington, University of Wisconsin, Vanderbilt University, and Yale University.

Software: `asfgrid` (Sharma & Stello 2016), `emcee` (Foreman-Mackey et al. 2013), `NumPy` (Walt 2011), `pandas` (McKinney 2010; Reback et al. 2020), `Matplotlib` (Hunter 2007), `IPython` (Pérez & Granger 2007), `SciPy` (Virtanen et al. 2020).

Appendix

We model the distribution of the fractional uncertainties, $\sigma_{\langle\nu'_{\max}\rangle}/\langle\nu'_{\max}\rangle$ and $\sigma_{\langle\Delta\nu'\rangle}/\langle\Delta\nu'\rangle$, as a function of the number of pipelines used to compute the uncertainties, dof, and evolutionary state (RGB or RGB/AGB versus RC). As described in the text, we use two generalized gamma distributions to model

each distribution of stars with a given dof (either 2, 3, 4, 5, or 6). When summed, the two fitted generalized gamma distributions are solutions to a least-squares minimization problem to describe the data, with Poisson uncertainties assumed for each bin in the observed distribution. To arrive at the fit, each component is weighted using a free parameter to describe the relative contribution of each component, and the degrees of freedom for each component are required to be less than or equal to the nominal degrees of freedom for the observed distribution (i.e., the number of reporting pipelines, dof). The solution is found using the Trust Region Reflective method as implemented in the `scipy` function, `curve_fit`. As a reference, we also fit each of the six distributions for both RGB or RGB/AGB and RC stars using a generalized gamma distribution with the uncertainty taken to be the median observed fractional uncertainty, and with the dof fixed to be the number of reporting pipelines. We do the same for the fractional uncertainty distributions for $\langle\kappa'_R\rangle$ and $\langle\kappa'_M\rangle$.

For $\langle\nu'_{\max}\rangle$ among RGB or RGB/AGB stars, the fractional uncertainties inferred from fitting the two-component generalized gamma distribution model vary according to the number of pipelines that contribute to the scatter estimate, from 1.1%–2.1%. For RC stars, the fitted uncertainties are larger and have a range of 2.2%–3.9%. The fitted fractional uncertainties on $\langle\Delta\nu'\rangle$ have marginally smaller fractional uncertainties, and they can range from 1.4% to 1.9% for RGB or RGB/AGB stars and from 1.9% to 2.8% for RC stars. For both $\langle\nu'_{\max}\rangle$ and $\langle\Delta\nu'\rangle$, therefore, the uncertainties vary more as a function of evolutionary state than number of pipelines reporting.

The uncertainty distributions for all of the RGB and RC stars are shown in Figures 20–21. We show both the expected distribution according to the observed median uncertainties using a fixed dof (gray curve), as well as the expected distribution from the two-component model (black curve), where we sum the uncertainties from each dof, weighting by the number of stars with a given dof. The agreement between the model for the uncertainties and the observed uncertainty distributions indicates that the uncertainties are largely not a function of ν_{\max} or $\Delta\nu$. Nevertheless, the approximation is not completely accurate: lower values of ν_{\max} and $\Delta\nu$ tend to have marginally larger fractional uncertainties—up to 1% larger across the entire observed parameter range for ν_{\max} and $\Delta\nu$ among RGB stars, and up to 3% larger for ν_{\max} among dof = 2 and dof = 3 RC stars with $\nu_{\max} < 30 \mu\text{Hz}$. (These latter low- ν_{\max} RC stars contribute to the extra bump at $\sigma_{\langle\nu'_{\max}\rangle}/\langle\nu'_{\max}\rangle \times 100 \approx 3$ in Figure 20.) The uncertainties are not strong functions of magnitude, which reflects the fact that the uncertainties are not dominated by white noise, but rather the length of the light curve, intrinsic properties of the star (e.g., evolutionary state), and pipeline agreement.

The $\langle\kappa'_M\rangle$ fractional uncertainties reinforce the trend for fractional uncertainties to vary more as a function of evolutionary state than a function of number of pipelines reporting: for RGB and RGB/AGB, the range is 6.2%–9.0%, and for RC stars, the range is 9.9%–12.1%. The uncertainty distributions of $\langle\kappa'_R\rangle$ and $\langle\kappa'_M\rangle$ for all of the RGB and RC stars are shown in Figures 22–23, where the gray and black curves correspond to the expected distribution according to the sample median uncertainties and the best-fitting uncertainties, which are obtained by appropriately weighted sums of the uncertainties at each dof.

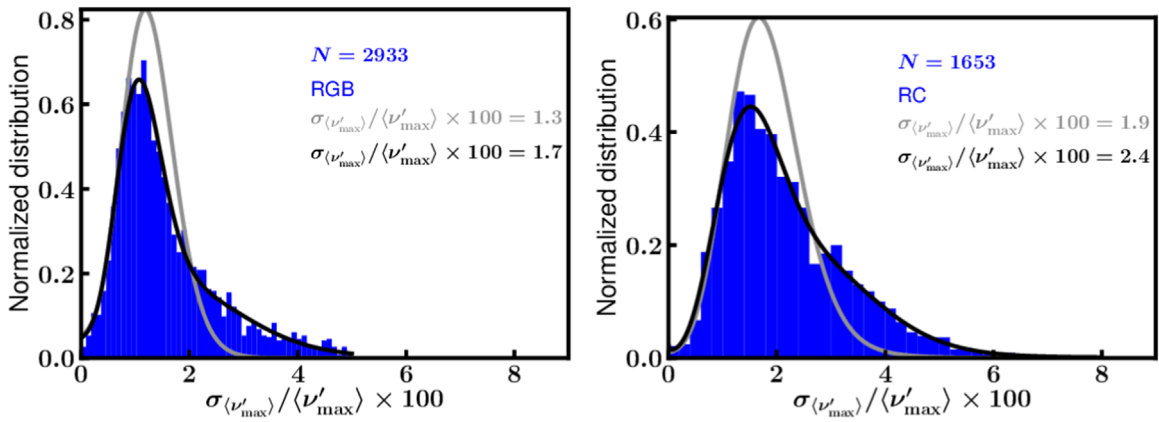


Figure 20. Left: Distribution of uncertainties in $\langle \nu'_{\max} \rangle$ for RGB stars, with curves showing models for the distributions assuming the median (gray) and best-fitting uncertainties (black)—the characteristic uncertainty according to each of these two models is shown in gray and black in the legend. These distributions and models are the results of summing the distributions and models for stars with dof = {2, 3, 4, 5, 6} pipelines reporting. Number of stars contributing to the observed distribution is listed as N . Right: same as left, but for RC stars.

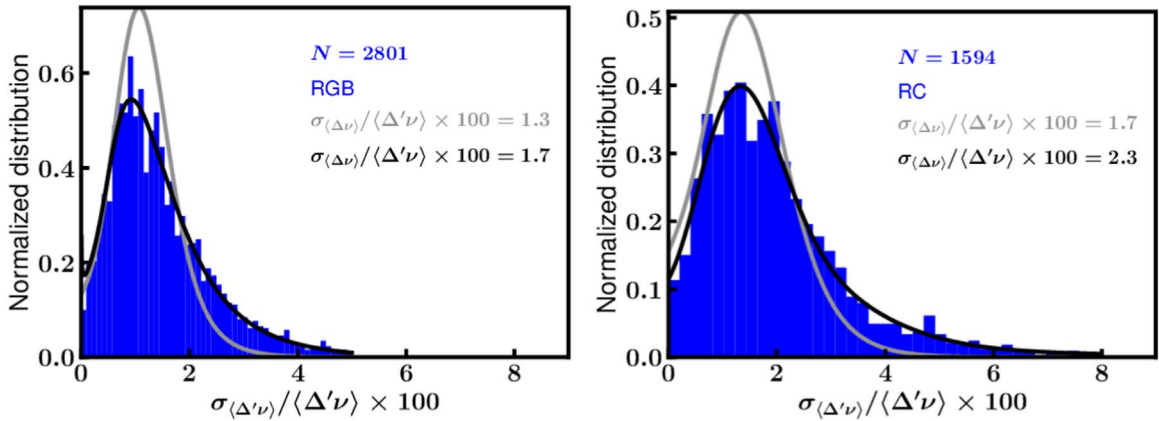


Figure 21. Left: same as Figure 20, but for $\langle \Delta \nu' \rangle$. Right: same as left, but for RC stars.

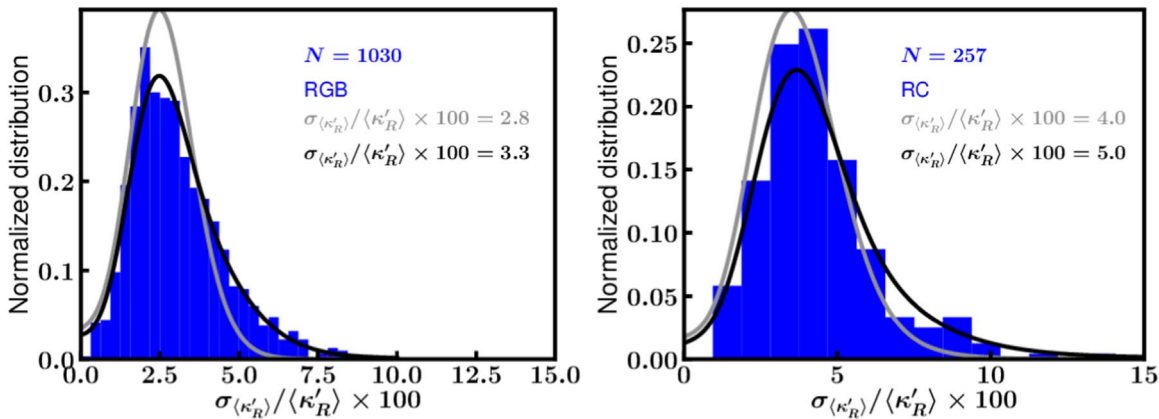


Figure 22. Left: same as Figure 20, but for $\langle \kappa'_R \rangle$. Right: same as left, but for RC stars.

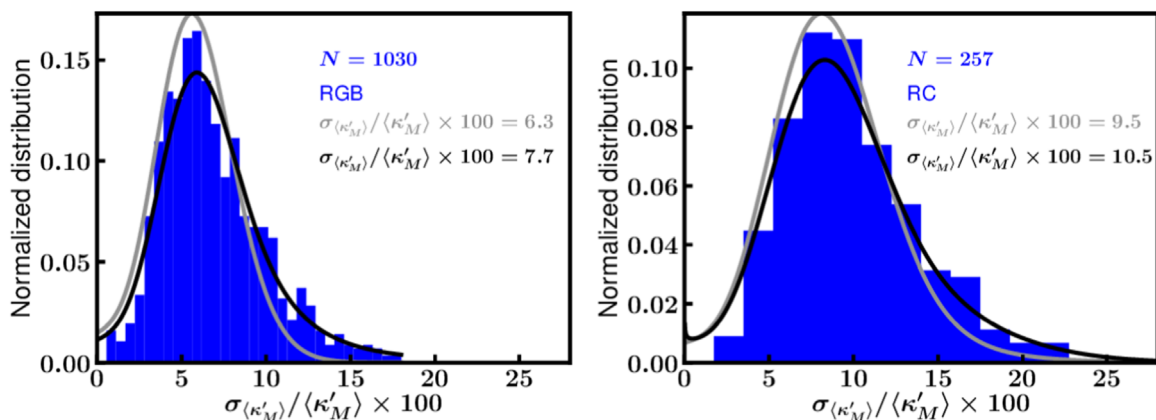


Figure 23. Left: same as Figure 22, but for $\langle \kappa'_M \rangle$. Right: same as left, but for RC stars.

ORCID iDs

Joel C. Zinn <https://orcid.org/0000-0002-7550-7151>
 Dennis Stello <https://orcid.org/0000-0002-4879-3519>
 Rafael A. García <https://orcid.org/0000-0002-8854-3776>
 Thomas Kallinger <https://orcid.org/0000-0003-3627-2561>
 Savita Mathur <https://orcid.org/0000-0002-0129-0316>
 Benoît Mosser <https://orcid.org/0000-0002-7547-1208>
 Lisa Bugnet <https://orcid.org/0000-0003-0142-4000>
 Marc Hon <https://orcid.org/0000-0003-2400-6960>
 Sanjib Sharma <https://orcid.org/0000-0002-0920-809X>
 Jack T. Warfield <https://orcid.org/0000-0003-1634-4644>
 Rodrigo Luger <https://orcid.org/0000-0002-0296-3826>
 Marc H. Pinsonneault <https://orcid.org/0000-0002-7549-7766>
 Jennifer A. Johnson <https://orcid.org/0000-0001-7258-1834>
 Daniel Huber <https://orcid.org/0000-0001-8832-4488>
 Victor Silva Aguirre <https://orcid.org/0000-0002-6137-903X>
 William J. Chaplin <https://orcid.org/0000-0002-5714-8618>
 Guy R. Davies <https://orcid.org/0000-0002-4290-7351>
 Andrea Miglio <https://orcid.org/0000-0001-5998-8533>

References

Ahumada, R., Prieto, C. A., Almeida, A., et al. 2020, *ApJS*, 249, 3
 An, D., Pinsonneault, M. H., Terndrup, D. M., & Chung, C. 2019, *ApJ*, 879, 81
 Bedding, T. R., Mosser, B., Huber, D., et al. 2011, *Natur*, 471, 608
 Belkacem, K., Goupil, M. J., Dupret, M. A., et al. 2011, *A&A*, 530, A142
 Borucki, W., Koch, D., Basri, G., et al. 2008, in IAU Symp. 249, Exoplanets: Detection, Formation and Dynamics, ed. Y.-S. Sun, S. Ferraz-Mello, & J.-L. Zhou (Cambridge: Cambridge Univ. Press), 17
 Bovy, J., Rix, H.-W., Green, G. M., Schlafly, E. F., & Finkbeiner, D. P. 2016, *ApJ*, 818, 130
 Brown, T. M., Gilliland, R. L., Noyes, R. W., & Ramsey, L. W. 1991, *ApJ*, 368, 599
 Bugnet, L., García, R. A., Davies, G. R., et al. 2018, *A&A*, 620, A38
 Casagrande, L., Silva Aguirre, V., Schlesinger, K. J., et al. 2016, *MNRAS*, 455, 987
 Chaplin, W. J., Houdek, G., Appourchaux, T., et al. 2008, *A&A*, 485, 813
 Chaplin, W. J., Kjeldsen, H., Bedding, T. R., et al. 2011, *ApJ*, 732, 54
 Elsworth, Y., Hekker, S., Johnson, J. A., et al. 2019, *MNRAS*, 489, 4641
 Elsworth, Y., Themeßl, N., Hekker, S., & Chaplin, W. 2020, *RNAAS*, 4, 177
 Foreman-Mackey, D., Hogg, D. W., Lang, D., & Goodman, J. 2013, *PASP*, 125, 306
 Gaia Collaboration, Brown, A. G. A., Vallenari, A., et al. 2018, *A&A*, 616, A1
 González Hernández, J. I., & Bonifacio, P. 2009, *A&A*, 497, 497
 Green, G. M., Schlafly, E. F., Finkbeiner, D. P., et al. 2015, *ApJ*, 810, 25
 Hall, O. J., Davies, G. R., Elsworth, Y. P., et al. 2019, *MNRAS*, 486, 3569

Hekker, S., Broomhall, A.-M., Chaplin, W. J., et al. 2010, *MNRAS*, 402, 2049
 Hon, M., Stello, D., & Yu, J. 2017, *MNRAS*, 469, 4578
 Hon, M., Stello, D., & Yu, J. 2018a, *MNRAS*, 476, 3233
 Hon, M., Stello, D., & Zinn, J. C. 2018b, *ApJ*, 859, 64
 Howell, S. B., Sobek, C., Haas, M., et al. 2014, *PASP*, 126, 398
 Huber, D., Bryson, S. T., Haas, M. R., et al. 2016, *ApJS*, 224, 2
 Huber, D., Ireland, M. J., Bedding, T. R., et al. 2012, *ApJ*, 760, 32
 Huber, D., Stello, D., Bedding, T. R., et al. 2009, *CoAst*, 160, 74
 Huber, D., Zinn, J., Bojsen-Hansen, M., et al. 2017, *ApJ*, 844, 102
 Hunter, J. D. 2007, *CSE*, 9, 90
 Kallinger, T., De Ridder, J., Hekker, S., et al. 2014, *A&A*, 570, A41
 Kallinger, T., Hekker, S., García, R. A., Huber, D., & Matthews, J. M. 2016, *SciA*, 2, 1500654
 Kallinger, T., Hekker, S., Mosser, B., et al. 2012, *A&A*, 541, A51
 Khan, S., Miglio, A., Mosser, B., et al. 2019, *A&A*, 628, A35
 Kjeldsen, H., & Bedding, T. R. 1995, *A&A*, 293, 87
 Kuszlewicz, J. S., Hekker, S., & Bell, K. J. 2020, *MNRAS*, 497, 4843
 Lindegren, L., Hernández, J., Bombrun, A., et al. 2018, *A&A*, 616, A2
 Luger, R., Kruse, E., Foreman-Mackey, D., Agol, E., & Saunders, N. 2018, *AJ*, 156, 99
 Majewski, S. R., Wilson, J. C., Hearty, F., Schiavon, R. R., & Skrutskie, M. F. 2010, in IAU Symp. 265, Chemical Abundances in the Universe: Connecting First Stars to Planets, ed. K. Cunha, M. Spite, & B. Barbuy (Cambridge: Cambridge Univ. Press), 480
 Mamajek, E. E., Prsa, A., Torres, G., et al. 2015, arXiv:1510.07674
 Martig, M., Mincev, I., & Flynn, C. 2014, *MNRAS*, 443, 2452
 Mathur, S., García, R. A., Régulo, C., et al. 2010, *A&A*, 511, A46
 Mathur, S., Hekker, S., Trampedach, R., et al. 2011, *ApJ*, 741, 119
 McKinney, W. 2010, in Proc. 9th Python in Science Conf., ed. S. van der Walt & J. Millman, 51, doi:10.25080/Majora-92bf1922-00a
 Miglio, A., Chiappini, C., Morel, T., et al. 2013, *MNRAS*, 429, 423
 Mosser, B., & Appourchaux, T. 2009, *A&A*, 508, 877
 Mosser, B., Belkacem, K., Goupil, M. J., et al. 2010, *A&A*, 517, A22
 Mosser, B., Michel, E., Samadi, R., et al. 2019, *A&A*, 622, A76
 Pérez, F., & Granger, B. E. 2007, *CSE*, 9, 21
 Pinsonneault, M. H., Elsworth, Y. P., Tayar, J., et al. 2018, *ApJS*, 239, 32
 Reback, J., McKinney, W., jbrockmendel, et al. 2020, pandas-dev/pandas: Pandas v1.1.4, Zenodo, doi:10.5281/zenodo.4161697
 Rendle, B. M., Miglio, A., Chiappini, C., et al. 2019, *MNRAS*, 490, 4465
 Salaris, M., Chieffi, A., & Straniero, O. 1993, *ApJ*, 414, 580
 Schönrich, R., & Aumer, M. 2017, *MNRAS*, 472, 3979
 Schönrich, R., McMillan, P., & Eyer, L. 2019, *MNRAS*, 487, 3568
 Sharma, S., Bland-Hawthorn, J., Johnston, K. V., & Binney, J. 2011, *ApJ*, 730, 3
 Sharma, S., & Stello, D. 2016, Asfgrid: Asteroseismic Parameters for a Star v0.0.5, Astrophysics Source Code Library, ascl:1603.009
 Sharma, S., Stello, D., Bland-Hawthorn, J., et al. 2019, *MNRAS*, 490, 5335
 Sharma, S., Stello, D., Bland-Hawthorn, J., Huber, D., & Bedding, T. R. 2016, *ApJ*, 822, 15
 Sharma, S., Stello, D., Buder, S., et al. 2018, *MNRAS*, 473, 2004
 Silva Aguirre, V., Bojsen-Hansen, M., Slumstrup, D., et al. 2018, *MNRAS*, 475, 5487
 Silva Aguirre, V., Casagrande, L., Basu, S., et al. 2012, *ApJ*, 757, 99
 Skrutskie, M. F., Cutri, R. M., Stiening, R., et al. 2006, *AJ*, 131, 1163
 Spitoni, E., Verma, K., Silva Aguirre, V., & Calura, F. 2020, *A&A*, 635, A58

- Stello, D., Huber, D., Sharma, S., et al. 2015, [ApJL](#), 809, L3
- Stello, D., Zinn, J., Elsworth, Y., et al. 2017, [ApJ](#), 835, 83
- Ulrich, R. K. 1986, [ApJL](#), 306, L37
- Vanderburg, A., & Johnson, J. A. 2014, [PASP](#), 126, 948
- Virtanen, P., Gommers, R., Oliphant, T. E., et al. 2020, [NatMe](#), 17, 261
- Walt, S. v. d., Colbert, S. C., & Varoquaux, G. 2011, [CSE](#), 13, 22
- Yu, J., Huber, D., Bedding, T. R., et al. 2018, [ApJS](#), 236, 42
- Zinn, J. C., Huber, D., Pinsonneault, M. H., & Stello, D. 2017, [ApJ](#), 844, 166
- Zinn, J. C., Pinsonneault, M. H., Huber, D., & Stello, D. 2019a, [ApJ](#), 878, 136
- Zinn, J. C., Pinsonneault, M. H., Huber, D., et al. 2019b, [ApJ](#), 885, 166
- Zinn, J. C., Stello, D., Huber, D., & Sharma, S. 2019c, [ApJ](#), 884, 107